

# Promising regions for detecting the overturning circulation in Atlantic Pa/Th: a model-data comparison

Jeemijn Scheen<sup>1,2,3</sup>, Jörg Lippold<sup>4</sup>, Frerk Pöppelmeier<sup>1,2</sup>, Finn Süfke<sup>4</sup>, Thomas  
F. Stocker<sup>1,2</sup>

<sup>1</sup>Climate and Environmental Physics, Physics Institute, University of Bern, Bern, Switzerland

<sup>2</sup>Oeschger Centre for Climate Change Research, University of Bern, Bern, Switzerland

<sup>3</sup>Department of Estuarine and Delta Systems, NIOZ Royal Netherlands Institute for Sea Research,

Yerseke, The Netherlands

<sup>4</sup>Institute of Earth Sciences, Heidelberg University, Heidelberg, Germany

## Key Points:

- We study the  $^{231}\text{Pa}/^{230}\text{Th}$  proxy for AMOC strength by comparing Bern3D model results to sediments from the Holocene and last glacial maximum
- Sensitive regions of  $^{231}\text{Pa}/^{230}\text{Th}$  to AMOC are the equatorial West Atlantic and the northern North Atlantic besides the Bermuda Rise
- Particle fluxes are highly dependent on AMOC and thus allow  $^{231}\text{Pa}/^{230}\text{Th}$  to even detect weak advection signals

---

Corresponding author: Jeemijn Scheen, [jeemijn.scheen@nioz.nl](mailto:jeemijn.scheen@nioz.nl)

## Abstract

The Atlantic Meridional Overturning Circulation (AMOC) is a critical component of the climate system, strongly influencing the climate via ocean heat transport. The AMOC had different characteristics during glacial periods and is expected to change under anthropogenic climate forcing. To reconstruct past AMOC strength, the Pa/Th (protactinium-231 to thorium-230) ratio measured in marine sediments serves as a unique proxy. However, this ratio reflects not only circulation changes, but also effects from biological particle export and benthic nepheloid layers. Therefore, it remains an open question which regions exhibit a reliable AMOC signal in their sedimentary Pa/Th. This study, utilising the Bern3D model and a compilation of sediment cores with 11 newly published cores, suggests that equatorial West Atlantic Pa/Th is as sensitive to AMOC changes as the Bermuda Rise region. Additionally, the Pa/Th response to AMOC changes observed in part of the northern North Atlantic, which is opposite to regions further south, is caused by AMOC-induced changes in particle production. Cores in this region are promising to reconstruct AMOC strength, despite exhibiting an AMOC-to-Pa/Th relationship opposite from usual and high levels of opal. Additional cores in the North Atlantic at 40–60°N between 1 and 2 km depth are desirable for the application of Pa/Th. Our results suggest a new focus of Pa/Th reconstructions on the equatorial West Atlantic and the northern North Atlantic, which appear to be better suited to quantify past AMOC strength.

## 1 Introduction

The strength of the Atlantic Meridional Overturning Circulation (AMOC) affects the climate in both hemispheres via ocean heat transport. There is an increasing body of evidence indicating that the AMOC experienced rapid variations in the past, for instance during the last deglaciation (Lynch-Stieglitz, 2017; Gebbie, 2014; Pöppelmeier et al., 2021; Repschläger et al., 2021). To reconstruct past AMOC strength, the ratio of protactinium-231 to thorium-230 (Pa/Th hereafter) measured in deep sea sediments is frequently used (McManus et al., 2004; Lippold et al., 2012a; Bradtmiller et al., 2014; Ng et al., 2018). Since the first reconstructions, the Pa/Th records from the Northwest Atlantic Bermuda Rise are often considered as the standard Pa/Th time series over the last 20,000 years and are commonly interpreted as inverse AMOC strength (McManus et al., 2004; Henry et al., 2016; Böhm et al., 2015; Lippold et al., 2019). There are, however, still open questions on biases concerning the Pa/Th proxy such as the impact of variable particle fluxes and bottom scavenging, with the latter being strongly present in the Bermuda Rise region (Lerner et al., 2020; Gardner et al., 2018b). In addition, certain regions in the North Atlantic show a positive correlation between Pa/Th and AMOC strength (Süfke et al., 2020; Gherardi et al., 2009), instead of the negative correlation as observed in the Bermuda Rise record. In summary, interpreting Bermuda Rise Pa/Th as a pure AMOC signal remains debated, while interpreting Pa/Th records from other regions appears to be even more challenging.

Pa and Th are both decay products of dissolved uranium, which is well-mixed in the ocean, such that the production rate of both isotopes is spatiotemporally constant at a Pa to Th ratio of 0.093 (Chen et al., 1986). In contrast to uranium, dissolved Pa and Th are both highly particle reactive with Pa binding less well to particles than Th. In their particle-bound form, Pa and Th sink along with the particles to the sediment (Fig. 1). Dissolved Pa has a longer residence time than Th such that it can be transported away from its production site. For instance, in the North Atlantic Pa is advected southwards along with North Atlantic Deep Water (NADW) if the AMOC is strong. So if the AMOC strength increases, more dissolved Pa is transported away out of the North Atlantic, and a sediment core in the North Atlantic will record a larger deficit in Pa and hence a lower Pa/Th ratio. This explains the anti-correlation between Pa/Th and AMOC strength in the studies on this proxy at the Bermuda Rise. The main sink of Pa and Th is adsorption to and sinking along with biogenic or lithogenic particles through the water column towards the sediment (Anderson et al., 1983). The adsorption (or ‘scavenging’) to particles is reversible (Bacon & Anderson, 1982): a continuous exchange occurs from dissolved to particle-bound forms (adsorption onto particles) and vice versa (desorption from particle surfaces). This chemical equilibrium would establish on a time scale of a few months (Bacon & Anderson, 1982; Henderson et al., 1999), but is continuously disturbed by other processes (see Fig. 1). Different particle types have different scavenging behaviour for Pa and Th. This poses a challenge for interpreting Pa/Th since particle distributions differ between regions and over time. Other particle types have been observed to play a role in the cycling of Pa and Th as well, such as particles from riverine input and hydrothermal vents (Fe-Mn oxyhydroxides) (Hayes et al., 2015a). Moreover, only few constraints are yet available for these particle types, which would not facilitate a global-scale implementation and we therefore do not consider them here. Further sinks are scavenging by nepheloid-layer particles close to the seafloor, also called bottom scavenging (Deng et al., 2014; Okubo et al., 2012), and radioactive decay with half-lives of 32.8 ka ( $^{231}\text{Pa}$ ) and 75.6 ka ( $^{230}\text{Th}$ ), which are negligible compared to the other sinks in the modern ocean. Finally, particle-bound Pa and Th also transform back to their dissolved forms when particles remineralise at depth.

Simulating the cycles of Pa and Th in the oceans received increasing attention in the last decade (Rempfer et al., 2017; Gu & Liu, 2017; van Hulten et al., 2018; Gu et al., 2020; Lerner et al., 2020; Missiaen et al., 2020a, 2020b; Chen et al., 2021; Luo et al., 2021; Sasaki et al., 2022), with Pa and Th tracers now implemented in a number of ocean models. Early box modelling already established a firm understanding of reversible scavenging of Th (Bacon & Anderson, 1982), which was later implemented for Pa and Th in 2D (Luo et al., 2010), in 2.5D (Marchal et al., 2000), in 3D inverse models (Marchal et al., 2007; Burke et al., 2011) and in 3D dynamical ocean models (Henderson et al., 1999; Siddall et al., 2005; Dutay et al., 2009; Gu & Liu, 2017; Rempfer et al., 2017; Missiaen et al., 2020a; Lerner et al., 2020; Sasaki et al., 2022). For 3D models with a dynamically simulated ocean, two main implementations to simulate Pa and Th exist. We refer to these here as the ‘diagnostic’ and the ‘prognostic’ approach, based on the type

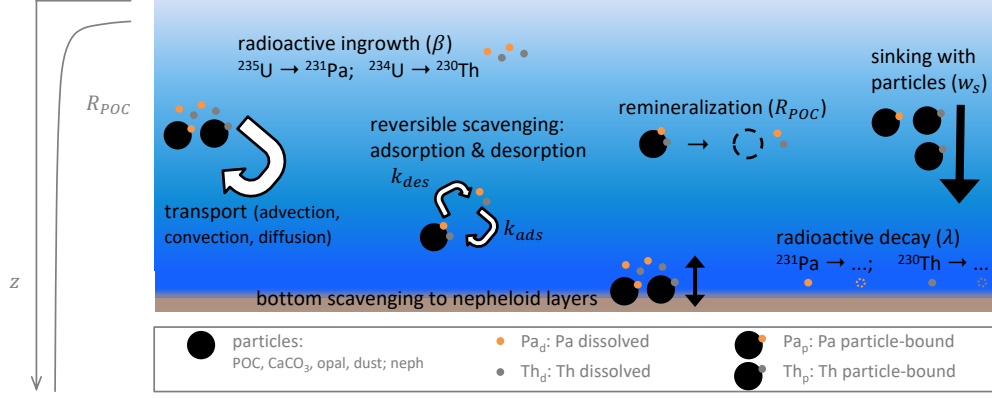


**Figure 1.** Schematic remineralisation profile function  $R_{POC}(z)$  (left) and processes of the protactinium and thorium cycle (right). Black circles in the ocean interior represent biogenic particles (POC,  $\text{CaCO}_3$ , opal) and dust, whereas black circles at the bottom are nepheloid-layer particles. Each process is simulated in the Bern3D model and has a corresponding term in Eq. (5)-(6). Symbols are listed in Table 1.

of their governing equations for Pa and Th (Appendix A). Briefly, the diagnostic approach assumes instantaneous equilibrium between dissolved and particle-bound phases, whereas the prognostic approach allows for an evolution towards adsorption-desorption equilibria over time and a possible influence by other processes, such as diffusion transporting dissolved Pa or Th away from their formation sites before equilibrium is reached.

Many of these previous modelling studies investigated the response of a weakened AMOC on sedimentary Pa/Th. These studies consistently found that the Pa/Th ratio increases in most of the North Atlantic and decreases in the South Atlantic, as the southwards transport of Pa is curtailed during weaker AMOC states (e.g., Marchal et al. (2000); Rempfer et al. (2017); Gu and Liu (2017); Missiaen et al. (2020a)). The scavenging parameters in models were tuned to observations by Marchal et al. (2000), Rempfer et al. (2017) and Missiaen et al. (2020a), but they found no consensus due to differences in approach, observational datasets and between models. Some studies investigated which particle types are most important for Pa/Th and they found a key role for opal (e.g., Siddall et al. (2005); Missiaen et al. (2020b)). Moreover, the studies by Rempfer et al. (2017) and Lerner et al. (2020) highlighted the importance of incorporating bottom scavenging to achieve a good representation of the modern distributions of dissolved Pa and Th.

In this study, we employ a state-of-the-art Pa/Th implementation in the Bern3D model, which we have tuned to match modern observations (GEOTRACES Intermediate Data Product Group, 2021; Deng et al., 2018; Ng et al., 2020; Pavia et al., 2020). We have added spatially resolved nepheloid layers to the model, which are important for bottom scavenging. As the first study, we deliberately added bottom scavenging before tuning particle scavenging coefficients. In a number of experiments, we explore the impact of varying AMOC, particle fluxes or both simultaneously. This enables us to esti-

**Table 1.** Parameters and variables of the protactinium-thorium module.

Symbol	Variable	Value	Unit
$i$	Particle type index	POC, $\text{CaCO}_3$ , opal, dust or neph	-
$j$	Nuclide index	$^{231}\text{Pa}$ or $^{230}\text{Th}$	-
$\text{Pa}_d$	Activity of dissolved Pa	simulated (Eq. (5))	$\mu\text{Bq/kg}$
$\text{Th}_d$	Activity of dissolved Th	simulated (Eq. (5))	$\mu\text{Bq/kg}$
$\text{Pa}_p$	Activity of particle-bound Pa	simulated (Eq. (6))	$\mu\text{Bq/kg}$
$\text{Th}_p$	Activity of particle-bound Th	simulated (Eq. (6))	$\mu\text{Bq/kg}$
$\beta^{Pa}$	Radioactive production of $^{231}\text{Pa}$ from U	$2.33 \cdot 10^{-3}$	$\text{dpm m}^{-3} \text{ yr}^{-1}$
$\beta^{Th}$	Radioactive production of $^{230}\text{Th}$ from U	$2.52 \cdot 10^{-2}$	$\text{dpm m}^{-3} \text{ yr}^{-1}$
$\lambda^{Pa}$	Decay constant of $^{231}\text{Pa}$	$2.13 \cdot 10^{-5}$	$\text{yr}^{-1}$
$\lambda^{Th}$	Decay constant of $^{230}\text{Th}$	$9.22 \cdot 10^{-6}$	$\text{yr}^{-1}$
$w_s$	Uniform sinking speed of particles	1600	$\text{m/yr}$
$k_{des}^j$	Desorption constant	4.0	$\text{yr}^{-1}$
$k_{ads}^j(\theta, \phi, z)$	Adsorption constant	Eq. (7)	$\text{yr}^{-1}$
$\sigma_i^j$	Scavenging coefficients	Table 3	see Table 3
$R_i(z)$	Remineralisation function	Eq. (2)-(4)	-
$F_i(\theta, \phi, z)$	Downward particle flux (for $i \neq \text{neph}$ )	Eq. (1); Fig. 2a-d	see Fig. 2a-d
$F_{ne}(\theta, \phi, z)$	Downward particle flux (for $i = \text{neph}$ )	Eq. (9)	$\text{g neph m}^{-2} \text{ yr}^{-1}$
$H_{ne}(\theta, \phi)$	Thickness of nepheloid layer	Fig. 2e	m
$m_{ne}^{tot}(\theta, \phi)$	Mass of nepheloid-layer particles, integrated over layer	Fig. 2f	$\text{g neph m}^{-2}$

mate sensitivities of regional Pa/Th to changes in AMOC strength. Comparisons to water column and sedimentary Pa/Th measurements help to build confidence in the model, and allow us to identify why certain regions carry a Pa/Th signal that correlates positively with AMOC strength while others are characterised by a negative correlation.

## 2 Methods

### 2.1 The Bern3D model

We employ the Bern3D Earth system Model of Intermediate Complexity, version 2.0, which has a grid resolution of  $41 \times 40$  in longitude by latitude, 32 ocean depth layers and a time step of 3.8 days (Roth et al. (2014), Appendix). The model contains coupled components for the ocean, land, and atmosphere, which exchange fluxes of heat, evaporation minus precipitation and carbon. The ocean is dynamically simulated based on frictional geostrophic balance equations (Edwards et al., 1998; Müller et al., 2006). A monthly wind climatology (Kalnay et al., 1996) applies wind stress to the surface ocean, whereas sea-ice growth, melt and advection are dynamically simulated. The simplified atmosphere consists of a single-layer energy-moisture balance model (Ritz et al., 2011) with prescribed albedo. Export production is simulated for particulate organic carbon

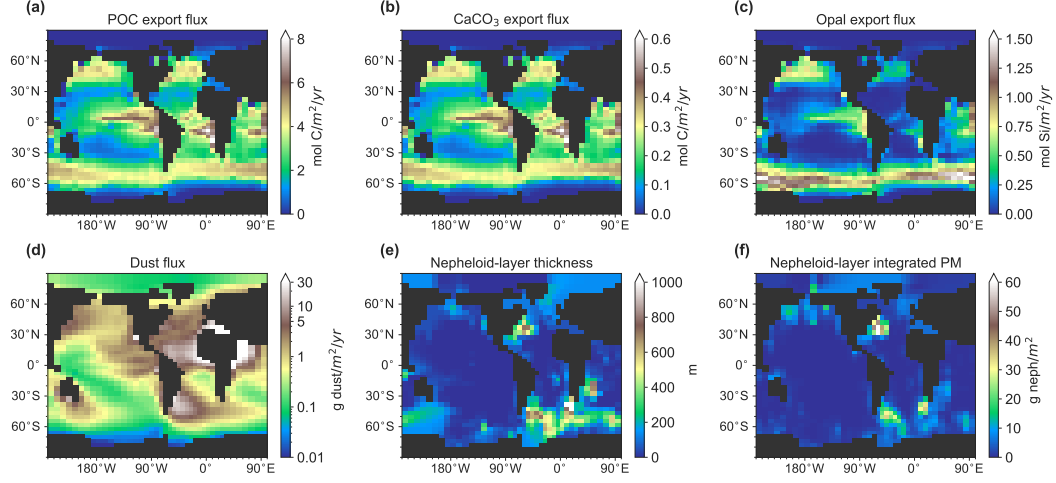


**Figure 2.** Particle export flux  $F_i(\theta, \phi, z_{eu})$  at the bottom of the euphotic zone ( $75m$ ) as simulated by the Bern3D biogeochemical module at pre-industrial steady state for (a) particulate organic carbon, (b) calcium carbonate and (c) opal. (d) Dust export flux  $F_{du}(\theta, \phi, z)$  based on observations (Mahowald et al., 2006) on a logarithmic colour scale. Mean annual export fluxes are shown, while in model simulations a seasonal cycle is present for (a)-(d). Note the different colour scales and different units. (e) Nepheloid-layer thickness  $H_{ne}(\theta, \phi)$  and (f) excess particulate matter (PM) mass  $m_{ne}^{tot}(\theta, \phi)$  based on Gardner et al. (2018a).

(POC),  $\text{CaCO}_3$  and biogenic opal in the surface ocean (Parekh et al., 2008) based on light, nutrient limitation, temperature and dissolved inorganic carbon concentrations, which results in the steady state export fluxes as shown in Fig. 2a-c under pre-industrial conditions (annual average). The implementation of  $\text{CaCO}_3$  in the model is simplified and based on the simulated POC export scaled by a factor 0.075. Particle fluxes  $F_i(\theta, \phi, z)$  of particle type  $i$  remineralise instantaneously below the euphotic zone following the Martin-curve (Martin et al., 1987) for POC and exponential decays for  $\text{CaCO}_3$  and biogenic opal (Rempfer et al., 2011):

$$F_i(\theta, \phi, z) = F_i(\theta, \phi, z_{eu}) \cdot R_i(z) \quad (1)$$

for  $z > z_{eu} = 75m$ , where  $F_i(\theta, \phi, z_{eu})$  is the export flux at the base of the euphotic zone,  $z = z_{eu}$ , and  $R_i(z)$  is a remineralisation function between 0 and 1:

$$R_{POC}(z) = \left( \frac{z}{z_{eu}} \right)^{-\alpha}, \quad (2)$$

$$R_{ca}(z) = \exp\left(-\frac{z - z_{eu}}{l_{ca}}\right), \quad (3)$$

$$R_{op}(z) = \exp\left(-\frac{z - z_{eu}}{l_{op}}\right). \quad (4)$$

with exponent  $\alpha = 0.83$  (Roth et al., 2014) and length scales  $l_{ca} = 5066m$  (Jeltsch-Thömmes et al., 2019) and  $l_{op} = 10,000m$  (Tschumi et al., 2008).

## 2.2 Model development of Pa and Th tracers

We simulate Pa and Th with the prognostic approach, which is physically more realistic than the diagnostic approach. Variables and parameters are listed in Table 1. We report specific activities  $A$  (for simplicity called concentrations in this study) in  $\mu\text{Bq kg}^{-1}$  for easier comparability to seawater observations. Dissolved concentrations of Pa and Th are denoted throughout this study with the subscript d and particle-bound concentrations with subscript p. In equations, we abbreviate activities (concentrations) of dissolved forms as  $A_d^j$  with  $j \in [Pa, Th]$  and particle-bound forms as  $A_p^j$ . Compared to Rempfer et al. (2017), we improved the effect of remineralisation on Pa and Th, added dust as another scavenging particle type, updated bottom scavenging due to nepheloid layers and performed a systematic tuning of the scavenging coefficients to new observations (Sect. 2.5) and removed explicit boundary scavenging.

Sinking particles that are remineralised release their associated  $\text{Pa}_p$  or  $\text{Th}_p$  to the dissolved form. This was not accounted for in the previous model formulation of Rempfer et al. (2017). The Bern3D model assumes instantaneous export and remineralisation with remineralisation functions  $R_i(z)$ . For Pa and Th in the new remineralisation term, we make the approximation that all  $A_p^j$  is bound to POC because POC export dominates in most regions (Fig. 2a-c). We convert  $R_{POC}(z)$  to a remineralisation rate  $\mu_{POC}(z)$  in  $\text{yr}^{-1}$ : the fraction of POC that is remineralised inside the grid cell layer at depth  $k$  is  $R_{POC}(k-1) - R_{POC}(k)$  – this takes place during the time  $t_k = \Delta z(k)/w_s$  that the sinking particles are inside this layer. Thus, the fraction of  $A_p^j$  transformed into  $A_d^j$  by remineralisation is  $\mu_{POC}(k) = [R_{POC}(k-1) - R_{POC}(k)]/\Delta z(k) \cdot w_s \approx -w_s \cdot \partial R_{POC}(z)/\partial z$  in  $\text{yr}^{-1}$ . The conversion of  $A_p^j$  to  $A_d^j$  under remineralisation can now be parametrised with a term  $\mu(z) \cdot A_p^j$  (Nickelsen et al., 2015). With this extra remineralisation term, the governing equations in our simulations become

$$\frac{\partial A_d^j}{\partial t} = \text{Transport}(A_d^j) - \lambda^j A_d^j + k_{\text{des}}^j A_p^j - k_{\text{ads}}^j A_d^j - w_s \frac{\partial R_{POC}(z)}{\partial z} A_p^j + \beta^j, \quad (5)$$

$$\frac{\partial A_p^j}{\partial t} = \text{Transport}(A_p^j) - \lambda^j A_p^j - k_{\text{des}}^j A_p^j + k_{\text{ads}}^j A_d^j + w_s \frac{\partial R_{POC}(z)}{\partial z} A_p^j - w_s \frac{\partial A_p^j}{\partial z}. \quad (6)$$

The tracers are subject to oceanic transport (advection, convection and diffusion). Sources and sinks are: radioactive decay  $\lambda^j$ , production by decay from a parent nuclide  $\beta^j$  and scavenging by sinking particles with sinking speed  $w_s$  (last term of Eq. (6)). Scavenging is parameterised via adsorption and desorption coefficients:

$$k_{\text{ads}}^j(\theta, \phi, z) = \sum_i \sigma_i^j \cdot F_i(\theta, \phi, z), \quad (7)$$

$$k_{\text{des}}^j = 4.0 \text{ yr}^{-1}, \quad (8)$$

$$i \in [POC, \text{CaCO}_3, \text{opal}, \text{dust}, \text{neph}]$$

$$j \in [Pa, Th]$$

where  $\sigma_i^j$  are globally fixed scavenging coefficients expressing how strongly particle type  $i$  adsorbs tracer  $j$ .

Lithogenic particles in the form of dust and nepheloid-layer are also considered in Eq. (7). Dust fields are prescribed after the model output from Mahowald et al. (2006), whereas nepheloid-layer concentrations and thickness are derived from Gardner et al. (2018a). We assume no remineralisation of dust and nepheloid-layer particles, because they dissolve little while sinking through the water column to the sediment (Carroll & Starkey, 1958). The spatial distribution of nepheloid layers is based on nephelometer and transmissometer data by Gardner et al. (2018a). The authors provide thicknesses of nepheloid layers,  $H_{ne}$ , and excess particulate matter mass (i.e., in excess to biological particles and dust) integrated over the nepheloid-layer height,  $m_{ne}^{tot}$ . We combine these two quantities to find a flux  $F_{ne}(\theta, \phi, z)$ . We use for  $H_{ne}$  the transmissometer results (their Fig. 2a), because they are derived from data with a better depth resolution, and for  $m_{ne}^{tot}$  we take the combination of transmissometer and nephelometer data (their Fig. 3c), which is available in this case. These variables were regridded and data gaps were filled (see Supplementary Text S1).

We distribute the integrated excess particulate matter,  $m_{ne}^{tot}(\theta, \phi)$ , uniformly over the height of the nepheloid layer,  $H_{ne}(\theta, \phi)$ , yielding a nepheloid particulate matter concentration of  $m_{ne}^{tot}(\theta, \phi)/H_{ne}(\theta, \phi)$  throughout the nepheloid-layer part of a water column. This simplification only has a small impact as the nepheloid layer consists of a maximum of three vertical grid cells in the open ocean (grid cells are particularly high close to the bottom: up to 400m at 5km depth). Converting concentration to flux via the sinking speed  $w_s$ , which we take identical as for the other particles, gives:

$$F_{ne}(\theta, \phi, z) = \frac{w_s \cdot m_{ne}^{tot}(\theta, \phi)}{H_{ne}(\theta, \phi)} \quad (9)$$

for  $z$  in the nepheloid layer ( $F_{ne} = 0$  elsewhere). This  $F_{ne}(\theta, \phi, z)$  is then used in Eq. (7).

### 2.3 Seawater data

Seawater data from the GEOTRACES Intermediate Data Product Group (2021), from Deng et al. (2018); Ng et al. (2020) and Pavia et al. (2020) were used for model tuning. These consist of measurements of  $\text{Pa}_d$ ,  $\text{Th}_d$ ,  $\text{Pa}_p$  and  $\text{Th}_p$  taken from 2008 to 2020. We excluded the Arctic basin, as the Arctic water mass cannot be realistically simulated with the coarse resolution of the Bern3D model.

We used all available measurements from Deng et al. (2018); Ng et al. (2020) and Pavia et al. (2020). The GEOTRACES Intermediate Data Product Group (2021) measurements were performed by Venchiarutti et al. (2011); Hayes et al. (2013); Deng et al. (2014); Hayes et al. (2015b, 2015a); Anderson et al. (2016); Hayes et al. (2017); Roy-Barman et al. (2019); Pavia et al. (2019). For dissolved Pa and Th, we only considered measurements from bottles (98 % of all measurements) and those labelled as “good quality” (98



% of the bottle measurements). Three types of measured particulate Pa and Th data are available from the data product, all from in situ filtration (pump). We used all these types together as Pa<sub>p</sub> and Th<sub>p</sub>, using only those labelled good quality (99 %).

In total, we used 1646 Pa<sub>d</sub> (1857 Th<sub>d</sub>) seawater measurements from 122 (151) stations. For Pa<sub>p</sub> we used 548 (for Th<sub>p</sub> 648) seawater measurements from 50 (59) stations. Reported uncertainties were on average 6 %, 4 %, 11 % and 5 % of measured values for Pa<sub>d</sub>, Th<sub>d</sub>, Pa<sub>p</sub> and Th<sub>p</sub>, respectively. If multiple measurements fell in the same model grid cell, they were combined into a single value  $obs_l$  (used later in Eq. (11)) by averaging with weights  $a_{i,l} = 1/e_{i,l}$  with  $e_{i,l}$  the uncertainty of a single observation  $i$  in grid cell  $l$ . Measurement uncertainties were propagated as appropriate for weighted averages:

$$e_l = \frac{\sqrt{\sum_{i=1}^M (a_{i,l})^2 \cdot (e_{i,l})^2}}{\sum_{i=1}^M a_{i,l}}, \quad (10)$$

where  $M$  is the number of measurements in grid cell  $l$ . This collection of seawater data was used for model tuning (Sect. 2.5 and Supplementary Text S2) and is partially shown in Fig. 5, C1 and Supplementary Fig. S5-S7 as model-data comparison.

## 2.4 New and published sediment data

For this study, we compiled Atlantic  $^{231}\text{Pa}_p/^{230}\text{Th}_p$  records combining data from 104 published sediment cores and 11 new records (Fig. 3a). The new cores improve the spatial coverage of the data set available from the literature, in particular filling gaps over a wide range of water depths in the South Atlantic.

For the new  $^{231}\text{Pa}/^{230}\text{Th}$  records, sediment samples have been analysed for the concentration of the radioisotopes  $^{230}\text{Th}$ ,  $^{231}\text{Pa}$ ,  $^{232}\text{Th}$ ,  $^{234}\text{U}$ , and  $^{238}\text{U}$ . Per sample approximately 0.1 g of sediment was weighed and then spiked with  $^{233}\text{Pa}$ ,  $^{229}\text{Th}$  and  $^{236}\text{U}$  prior to chemical treatment, followed by total digestion in a mixture of concentrated HCl, HNO<sub>3</sub> and HF. Purification and separation of Pa, Th and U followed the standard protocols described by Sufke et al. (2018). The short-lived  $^{233}\text{Pa}$  spike ( $t_{1/2} = 27$  days) was milked from a  $^{237}\text{Np}$  solution using the procedure described by Regelous et al. (2004). The  $^{233}\text{Pa}$  spike was calibrated against an internal pitchblende standard (Fietzke et al., 1999) and the reference material IAEA-385 (Sufke et al., 2018). Isotope measurements were performed on a Neptune Plus MC-ICP-MS in the Geozentrum Nordbayern at Erlangen, Germany, and on an iCAP TQe ICP-MS at the Institute of Earth Sciences of Heidelberg University.  $^{230}\text{Th}$ ,  $^{232}\text{Th}$  and  $^{238}\text{U}$  generally had full-process blank contributions lower than 1 %;  $^{231}\text{Pa}$  below 2 %. The desired excess fractions (i.e., the  $^{231}\text{Pa}$  and  $^{230}\text{Th}$  produced in the overlying water column from decay of dissolved uranium) were calculated from the measured total concentrations by correcting for detrital and authigenic input and radioactive decay since the time of deposition following the suggestions by Bourne et al. (2012).

**Table 2.** Sediment measurements. Index # and Region refer to Fig. 3; ‘Pa/Th’ is the average of ‘n’ samples in the time interval; SE is standard error. This table is also provided as Supplementary Dataset S1; individual samples of new cores are listed in Supplementary Dataset S2.

#	Core	Lat	Lon	Depth	Holocene (0-8 ka)			LGM (18-23 ka)			Reference	Region
					Pa/Th	n	SE	Pa/Th	n	SE		
1	MD95-2014	60.58	-22.08	2397	-	-	-	0.082	2	0.002	Lippold et al. (2012a)	
2	GS06-144-08GC	60.40	-23.63	1950	-	-	-	0.127	1	0.005	Lippold et al. (2012a)	
3	ODP 983	60.40	-23.64	1984	0.126	2	0.007	0.087	2	0.003	this study	
4	DACP2	58.97	-9.61	1709	0.093	4	0.002	0.057	1	0.015	Hall et al. (2006)	
5	MD95-2015	58.76	-25.96	2630	0.120	1	0.004	0.082	2	0.003	Lippold et al. (2012a)	
6	BOFS 17K	58.00	-16.50	1150	0.123	6	0.010	0.120	4	0.008	Roberts et al. (2014)	
7	GS06-144-02GC	57.48	-48.62	3440	0.110	1	0.003	-	-	-	Lippold et al. (2012a)	
8	BOFS 10K	54.70	-20.70	2777	0.073	8	0.003	-	-	-	Roberts et al. (2014)	
9	MD08-3182CQ	52.70	-35.94	3757	0.103	1	0.003	-	-	-	Lippold et al. (2012a)	
10	BOFS 8K	52.50	-22.06	4045	0.068	2	0.005	0.089	3	0.003	Roberts et al. (2014)	
11	SU90-44	50.20	-17.00	4279	0.051	5	0.005	0.079	2	0.002	Gherardi et al. (2009)	
12	SU90-102	45.09	-39.44	1965	0.091	9	0.023	0.092	4	0.029	Süfke et al. (2020)	1
13	SU90-11	44.07	-40.03	3645	-	-	-	0.067	5	0.007	Lippold et al. (2012a)	1
14	M45/5 KL86	43.37	-22.49	3028	-	-	-	0.065	1	0.003	Lippold et al. (2012a)	
15	GeoB18530-1	42.50	-49.14	1888	0.088	4	0.006	0.073	4	0.011	this study	
16	MD95-2027	41.70	-52.40	4112	-	-	-	0.080	2	0.004	Gherardi et al. (2009)	
17	SU90-09	43.08	-31.08	3375	-	-	-	0.058	1	0.002	Lippold et al. (2012a)	1
18	SU90-08	43.05	-30.04	3080	-	-	-	0.043	1	0.002	Lippold et al. (2012a)	1
19	IODP 1313	41.00	-32.96	3413	0.053	6	0.001	0.053	8	0.003	this study	1
20	MSM58-13-2	40.40	-31.08	2102	0.074	6	0.004	0.040	5	0.005	this study	1
21	SU90-03	40.31	-32.04	2475	0.057	6	0.003	0.044	9	0.005	this study	1
22	MSM58-28-4	38.58	-35.54	4110	0.050	3	0.001	0.064	9	0.004	this study	1
23	SU92-18	37.79	-27.23	2300	0.071	1	0.006	-	-	-	Lippold et al. (2012a)	
24	MD95-2037	37.10	-32.00	2159	0.094	7	0.007	0.046	4	0.009	Gherardi et al. (2009)	1
25	SU81-18	37.80	-10.20	3135	0.064	9	0.008	0.049	5	0.002	Gherardi et al. (2009)	
26	V27-263	35.02	-40.92	3704	0.037	1	0.001	0.040	1	0.003	Bradtmitter et al. (2014)	1
27	OCE326-GGC5	33.70	-57.60	4550	0.055	8	0.003	0.067	12	0.004	McManus et al. (2004)	2
28	ODP 1063	33.69	-57.61	4584	0.057	52	0.002	0.064	17	0.004	Lippold et al. (2019)	2
29	V29-172	33.70	-29.38	3457	0.054	1	0.001	0.052	3	0.003	Bradtmitter et al. (2014)	
30	ODP 1055	32.78	-76.29	1798	0.065	1	0.003	-	-	-	Lippold et al. (2012a)	2
31	KN140-2-51GGC	32.78	-76.28	1790	0.069	19	0.004	-	-	-	Hoffmann et al. (2018)	2
32	ODP 1056	32.48	-76.33	2166	0.059	1	0.002	-	-	-	Lippold et al. (2012a)	2
33	ODP 1058	31.69	-75.43	2984	0.060	1	0.003	-	-	-	Lippold et al. (2012a)	2
34	ODP 1059	31.67	-75.42	2985	0.060	7	0.008	0.065	6	0.008	Süfke et al. (2019)	2
35	KNR140 31GGC	30.90	-74.50	3410	0.066	1	0.003	0.134	1	0.020	Bradtmitter et al. (2014)	2
36	ODP 1060	30.76	-74.57	3481	0.056	5	0.003	0.077	5	0.003	Süfke et al. (2019)	2
37	ODP 1061	29.98	-73.60	4038	0.056	5	0.002	0.079	10	0.005	Süfke et al. (2019)	2
38	12JPC	29.75	-72.90	4250	0.060	3	0.001	0.074	4	0.003	Süfke et al. (2019)	2
39	ODP 1062	28.25	-74.41	4761	0.052	4	0.001	0.073	6	0.005	Süfke et al. (2019)	2
40	M45/5 KL90	31.61	-28.02	3143	-	-	-	0.048	1	0.001	Lippold et al. (2012a)	
41	V25-21	26.40	-45.45	3693	0.046	1	0.001	0.037	2	0.005	Bradtmitter et al. (2014)	
42	GeoB9508-5	15.50	-17.95	2384	0.109	3	0.010	0.060	3	0.001	Lippold et al. (2012b)	
43	Gramberg JC094-S0177-CT	15.46	-50.99	2714	0.061	1	0.002	-	-	-	Ng et al. (2020)	
44	JC094-GVY14	15.46	-50.99	2714	0.057	3	0.009	0.077	4	0.009	Ng et al. (2018)	
45	Gramberg JC094-S0170-CT	15.44	-51.10	1675	0.095	1	0.003	-	-	-	Ng et al. (2020)	
46	Gramberg JC094-S0161-CT	15.42	-51.09	1379	0.122	1	0.004	-	-	-	Ng et al. (2020)	
47	Vayda JC094-S0131-CT	15.17	-48.25	4126	0.055	1	0.002	-	-	-	Ng et al. (2020)	
48	Vayda JC094-S0138-CT	14.89	-48.12	1055	0.160	1	0.006	-	-	-	Ng et al. (2020)	
49	Vayda JC094-S0140-CT	14.85	-48.27	2166	0.074	1	0.002	-	-	-	Ng et al. (2020)	
50	Vayda JC094-S0157-CT	14.77	-48.25	3721	0.060	1	0.002	-	-	-	Ng et al. (2020)	
51	GeoB3936-1	12.72	-59.00	1854	0.078	1	0.003	-	-	-	Lippold et al. (2011)	
52	GeoB3935-2	12.61	-59.39	1558	0.082	1	0.004	-	-	-	Lippold et al. (2011)	
53	GeoB3937-2	12.56	-58.77	1654	0.079	1	0.003	-	-	-	Lippold et al. (2011)	
54	M35003	12.09	-61.24	1300	0.109	2	0.003	0.080	2	0.003	Lippold et al. (2016)	
55	Vema JC094-S0120-CT	10.78	-44.60	2932	0.071	1	0.003	-	-	-	Ng et al. (2020)	3
56 <sup>a</sup>	Vema JC094-S0114A-CT	10.73	-44.42	1094	0.209	1	0.006	-	-	-	Ng et al. (2020)	3
57 <sup>a</sup>	Vema JC094-S0119-CT	10.71	-44.42	570	0.268	1	0.008	-	-	-	Ng et al. (2020)	3
58	Carter JC094-S0021-CT	9.28	-21.64	4565	0.048	1	0.002	-	-	-	Ng et al. (2020)	
59	Carter JC094-S0058-CT	9.22	-21.31	684	0.228	1	0.007	-	-	-	Ng et al. (2020)	
60	Carter JC094-S0055-CT	9.21	-21.30	1366	0.199	1	0.006	-	-	-	Ng et al. (2020)	
61	Carter JC094-S0036-CT	9.18	-21.27	2719	0.082	1	0.003	-	-	-	Ng et al. (2020)	
62	Carter JC094-S0039-CT	9.17	-21.27	2278	0.104	1	0.004	-	-	-	Ng et al. (2020)	
63	JC094-GVY01	7.44	-21.80	3426	0.048	2	0.001	0.048	4	0.001	Ng et al. (2018)	
64	Carter JC094-S0066-CT	7.43	-21.80	3419	0.071	1	0.004	-	-	-	Ng et al. (2020)	
65	EW9209 1JPC	5.91	-44.20	4056	0.043	4	0.001	0.069	3	0.007	Ng et al. (2018)	3
66	Knipovich JC094-S0085-CT	5.71	-27.27	4405	0.045	1	0.002	-	-	-	Ng et al. (2020)	
67	Knipovich JC094-S0074-CT	5.63	-26.96	990	0.193	1	0.006	-	-	-	Ng et al. (2020)	
68	Knipovich JC094-S0071-CT	5.60	-26.97	1990	0.086	1	0.003	-	-	-	Ng et al. (2020)	
69	Knipovich JC094-S0080-CT	5.59	-26.99	2820	0.073	1	0.002	-	-	-	Ng et al. (2020)	
70	EW9209 3JPC	5.31	-44.26	3300	0.049	1	0.001	0.065	3	0.005	Ng et al. (2018)	3
71	38GGC	4.90	-20.50	2937	0.053	2	0.001	0.068	2	0.029	Lippold et al. (2012a)	
72	55GGC	4.90	-42.90	4556	0.045	2	0.002	0.067	3	0.008	Lippold et al. (2012a)	3
73	58GGC	4.80	-43.00	4341	0.045	3	0.009	0.072	3	0.013	Lippold et al. (2012a)	3
74	71GGC	4.40	-43.70	3164	0.059	2	0.001	0.053	1	0.003	Lippold et al. (2012a)	3
75	82GGC	4.30	-43.50	2816	0.049	3	0.004	0.051	1	0.003	Lippold et al. (2012a)	3
76	GeoB1515	4.24	-43.67	3129	0.051	2	0.008	0.077	3	0.003	Süfke et al. (2019)	3
77	GeoB1523	3.83	-41.62	3292	0.056	3	0.009	0.073	4	0.001	Süfke et al. (2019)	3
78	29GGC	2.50	-19.80	5105	0.043	3	0.003	0.061	2	0.018	Lippold et al. (2012a)	
79	RC13-189	1.86	-30.00	3233	0.054	3	0.003	0.067	3	0.001	Bradtmitter et al. (2007)	
80	RC16-66	-0.76	-36.62	4424	0.043	3	0.002	0.061	2	0.001	Bradtmitter et al. (2007)	3
81	RC24-01	0.56	-13.65	3837	0.042	2	0.001	0.059	1	0.003	Bradtmitter et al. (2007)	
82	V30-40	-0.20	-23.15	3706	0.034	3	0.001	0.050	3	0.009	Bradtmitter et al. (2007)	
83	V22-182	-0.53	-17.27	3614	0.034	3	0.010	0.057	2	0.001	Bradtmitter et al. (2007)	
84	RC24-07	-1.34	-11.92	3899	0.044	3	0.001	0.066	1	0.002	Bradtmitter et al. (2007)	
85	RC24-12	-3.01	-11.42	3486	0.045	3	0.002	0.058	2	0.002	Bradtmitter et al. (2007)	
86	GeoB16206-1	-1.58	-43.02	1367	-	-	-	0.092	3	0.024	Voigt et al. (2017)	
87	GeoB16202-2	-1.91	-41.59	2248	0.053	2	0.003	0.071	4	0.009	Mulitz et al. (2017)	3
88	MD3253	-2.35	-35.45	3867	0.042	1	0.002	-	-	-	Lippold et al. (2011)	3
89	MD3254	-2.80	-35.42	3715	0.042	1	0.002	-	-	-	Lippold et al. (2011)	3
90	MD09-3256Q	-3.55	-35.38	3537	0.047	1	0.002	-	-	-	Lippold et al. (2011)	3
91	MD3242	-4.22	-37.83	1008	0.090	1	0.005	-	-	-	Lippold et al. (2011)	3
92	MD09-3257	-4.24	-36.35	2344	0.067	3	0.006	0.085	11	0.021	Burckel et al. (2015)	3
93	GeoB3910	-4.25	-36.35	2362	0.057	1	0.001	0.075	1	0.003	Waelbroeck et al. (2018)	3
94	GeoB1035-4	-21.60	5.03	4450	0.031	1	0.001	0.039	2	0.001	Lippold et al. (2012a)	
95	GeoB1711-4	-23.34	12.38	1967	0.123	3	0.006	0.097	10	0.006	Lippold et al. (2012b)	
96	GeoB3722-2	-25.25	12.02	3506	0.065	3	0.001	0.106	7	0.004	Lippold et al. (2012b)	
97	C1 PC-ENG-111	-22.50	-40.10	621	0.097	1	0.003	0.117	2	0.005	Lippold et al. (2012a)	4
98	GeoB2117	-23.04	-36.65	4045	0.049	1	0.001	-	-	-	Hickey (2010)	4
99	C2 PC-2121009	-24.30	-43.20	781	0.098	1	0.008	-	-	-	Lippold et al. (2012a)	4
100	GeoB 2107	-27.18	-46.45	1048	0.0							

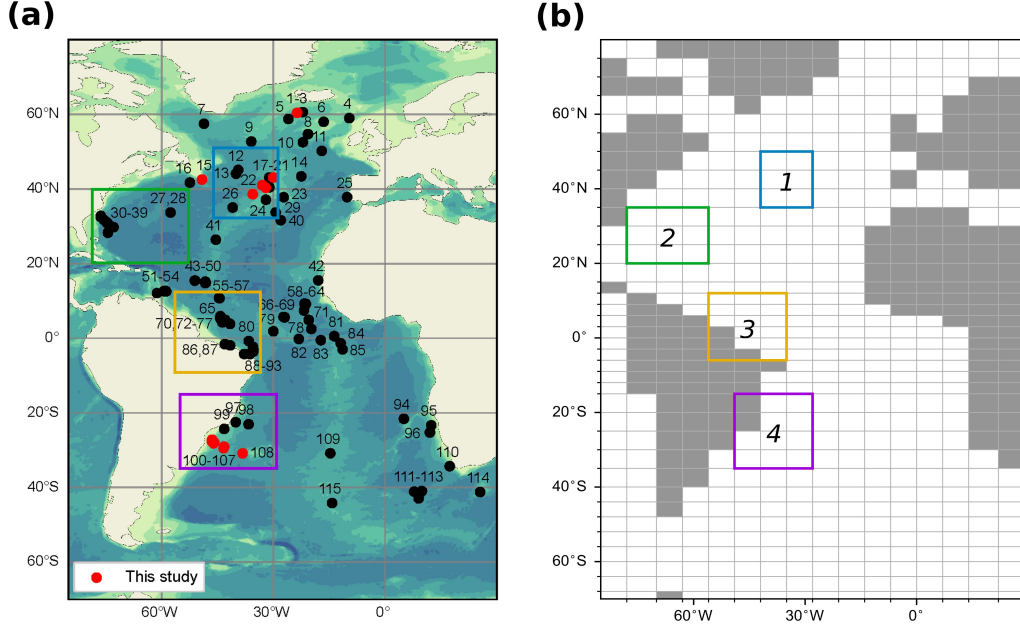


**Figure 3.** (a) Sediment cores used in this study. See also Table 2. Red circles are newly published cores. (b) Bern3D model grid in the Atlantic with the four regions of interest that are used in Fig. 10 and Fig. 12. Boundaries are 35–50°N, 42–28°W for region 1 (northern North Atlantic); 20–35°N, 78–56°W for region 2 (Bermuda Rise); 6°S–12°N, 56–35°W for region 3 (equatorial West Atlantic); and 35–15°S, 49–28°W for region 4 (Southwest Atlantic).

An overview of the observational  $^{231}\text{Pa}/^{230}\text{Th}$  database used for this study is provided in Table 2, indicating the Pa/Th average over the Holocene and Last Glacial Maximum samples. Published Holocene and LGM data of  $^{231}\text{Pa}/^{230}\text{Th}$ -records were used here from Anderson et al. (2014); Bradtmiller et al. (2007, 2014); Burckel et al. (2015); Gherardi et al. (2005, 2009); Hall et al. (2006); Hickey (2010); Hoffmann et al. (2018); Jonkers et al. (2015); Lippold et al. (2011, 2012a, 2012b, 2016, 2019); McManus et al. (2004); Mulitza et al. (2017); Negre et al. (2010); Ng et al. (2018, 2020); Roberts et al. (2014); Sfke et al. (2019); Sfke et al. (2020); Voigt et al. (2017); Waelbroeck et al. (2018). If multiple samples were available for one core, we averaged the measurements over the mid-to-late Holocene (0–8 ka) and the Last Glacial Maximum (18–23 ka). The standard error (SE) was computed as the standard deviation of the uncertainties of the  $n$  samples divided by  $\sqrt{n-1}$ . We considered Holocene data from 0 to 8 ka only in order to avoid data that are influenced by the higher deglacial AMOC variability, assuming a relatively stable AMOC during the Holocene (Hoffmann et al., 2018; Lippold et al., 2019).

The Holocene sediment database was used to validate the tuned model results at the pre-industrial and to identify regions and water depths of high sensitivity of  $^{231}\text{Pa}/^{230}\text{Th}$  to AMOC changes (Sect. 3.1). In a subsequent step the LGM data have been compared to the model outputs of different Bern3D AMOC scenarios (Sect. 3.4).

## 2.5 Model tuning of Pa and Th

We tuned the Pa and Th implementations to reflect modern seawater observations by varying the scavenging parameters. The realism of model simulations highly depends on these parameters: the 10 scavenging coefficients  $\sigma_i^j$  that determine adsorption, the 2 desorption constants  $k_{des}^j$  and the particle sinking speed  $w_s$ . Simulations with varying  $(w_s, k_{des}^j, \sigma_i^j)$  were run for 5000 years into steady state. The model-data agreement of each simulation was quantified by taking the weighted Mean Absolute Error (MAE) for each of the four variables  $\text{Pa}_d$ ,  $\text{Th}_d$ ,  $\text{Pa}_p$  and  $\text{Th}_p$ :

$$MAE := MAE(w_s, k_{des}^j, \sigma_i^j) = \frac{\sum_{l=1}^N a_l \cdot |sim_l - obs_l|}{\sum_{l=1}^N a_l}, \quad (11)$$

where  $l = (\theta, \phi, z)$  is a grid cell where observations are present; with a weight  $a_l = \frac{1}{e_l}$  with  $e_l$  the observational uncertainty;  $sim_l$  is the model simulation output and  $obs_l$  the measurement in grid cell  $l$ . Recall from Sect. 2.3 that multiple observations within one grid cell were averaged. We tuned Pa and Th by fixing the optimal parameters in three steps: 1)  $w_s$ , 2)  $k_{des}^j$  and 3) all  $\sigma_i^j$ . In the following we briefly describe the approach of these three steps (more information in Supplementary Text S2), whereas the tuning results are discussed in Sect. 3.1.

First, we tuned the particle sinking speed  $w_s$  via an ensemble of 511 runs, in which all parameters  $(w_s, k_{des}^j, \sigma_i^j)$  were varied. We only considered the MAEs of  $\text{Pa}_p$  and  $\text{Th}_p$  because they are directly related to  $w_s$  via the sinking term in Eq. (6) (a change in  $w_s$  causes a change in  $A_p^j$  that subsequently affects  $A_d^j$  via adsorption and desorption, but this highly depends on the  $\sigma_i^j$  values, which vary randomly in this ensemble, obscuring a clear comparison). Since  $\text{Pa}_p$  and  $\text{Th}_p$  prefer different values for  $w_s$ , we found a compromise by taking the normalised sum for each simulation:

$$MAE_{p,tot} = \frac{MAE_{\text{Pa}_p}}{MAE_{\text{Pa}_p}} + \frac{MAE_{\text{Th}_p}}{MAE_{\text{Th}_p}}, \quad (12)$$

where the bar indicates an average over all runs of this ensemble. Equation (12) was only used to determine  $w_s$ . Subsequently, we established the best  $k_{des}^j$  (Supplementary Fig. S2). Instead of varying  $k_{des}^j$  in one ensemble, we varied it in three sub-ensembles with different fixed background parameter sets of  $w_s$  and  $\sigma_i^j$  (see Table 3) to explore how these affect the optimal  $k_{des}^j$ . For this tuning step we only evaluated  $MAE_{\text{Pa}_d}$  and  $MAE_{\text{Th}_d}$ .

Finally, the  $\sigma_i^j$  were tuned in a 3000-member ensemble with  $w_s$  and  $k_{des}^j$  fixed to the optimal values as determined in the previous tuning steps. This ensemble had more members, because in this step 10 parameters were tuned simultaneously. The limits of the parameter space of the partition coefficients  $K_i^j$  were derived from observational studies. These studies either performed laboratory experiments (Geibert & Usbeck, 2004; Zhang et al., 2021), used Atlantic seawater measurements from GEOTRACES (Hayes et al., 2015a) or used sediment traps (Chase et al., 2002; Luo & Ku, 2004a). Their  $K_i^j$  estimates were converted to  $\sigma_i^j$  via Eq. (A9), and the minima and maxima are given in Table 3

**Table 3.** Values of the sinking speed  $w_s$ , desorption constants  $k_{des}^j$  and scavenging coefficients  $\sigma_i^j$  for: three parameter sets used for the tuning of  $k_{des}^j$  (Supplementary Fig. S2); minimum and maximum  $\sigma_i^j$  of observational estimates ( $K_i^j$  from Chase et al. (2002); Geibert and Usbeck (2004); Hayes et al. (2015a); Luo and Ku (2004a); Zhang et al. (2021); converted via Eq. (A9) – see Supplementary Dataset S3); values in three other modelling studies and in this study. Our  $\sigma_i^j$  tuning was performed from minimum obs. to twice maximum obs.

Parameter Unit	$w_s$ m/yr	$k_{des}^j$ /yr	$\sigma_{POC}^{Pa}$ m <sup>2</sup> /mol C	$\sigma_{ca}^{Pa}$ m <sup>2</sup> /mol C	$\sigma_{op}^{Pa}$ m <sup>2</sup> /mol Si	$\sigma_{du}^{Pa}$ m <sup>2</sup> /g dust	$\sigma_{ne}^{Pa}$ m <sup>2</sup> /g neph	$\sigma_{POC}^{Th}$ m <sup>2</sup> /mol C	$\sigma_{ca}^{Th}$ m <sup>2</sup> /mol C	$\sigma_{op}^{Th}$ m <sup>2</sup> /mol Si	$\sigma_{du}^{Th}$ m <sup>2</sup> /g dust	$\sigma_{ne}^{Th}$ m <sup>2</sup> /g neph
Parameter set 1 (tuning $k_{des}^j$ )	1000	<i>varies</i>	0.020	0.230	0.22	0.0044	0.028	0.084	3.97	0.110	0.0023	0.028
Parameter set 2 (tuning $k_{des}^j$ )	1400	<i>varies</i>	0.021	0.097	0.24	0.0028	0.026	0.210	1.73	0.029	0.0180	0.096
Parameter set 3 (tuning $k_{des}^j$ )	1600	<i>varies</i>	0.021	0.097	0.24	0.0028	0.026	0.210	1.73	0.029	0.0180	0.096
Min obs.	-	-	0.011	0.0007	0.00084	0.00001	0.00001	0.028	0.0023	0.0026	0.00009	0.00009
Max obs.	-	-	0.022	0.036	0.091	0.028	0.028	0.14	0.95	0.13	0.058	0.058
Marchal et al. (2000)	700	3.0	0.075	0.075	0.75	-	-	0.75	0.75	0.75	-	-
Rempfer et al. (2017) <sup>a</sup>	1000	2.4	1	0.1	0.1	-	0.1	1	1	0.1	-	1
Missiaen et al. (2020a) <sup>b</sup>	1000	2.4	1.55	0.22	2.80	-	-	5.47	9.21	1.38	-	-
This study (CTRL)	1600	4.0	0.043	0.058	0.15	0.0031	0.029 <sup>c</sup>	0.090	1.83	0.082	0.011	0.064

<sup>a</sup>Values of  $\sigma_i^j$  are corrected for typos in their equations (see Appendix B).

<sup>b</sup>Values of  $\sigma_i^j$  are converted to our units.

<sup>c</sup>This parameter value is not well constrained by our tuning; the MAEs are not sensitive to it.

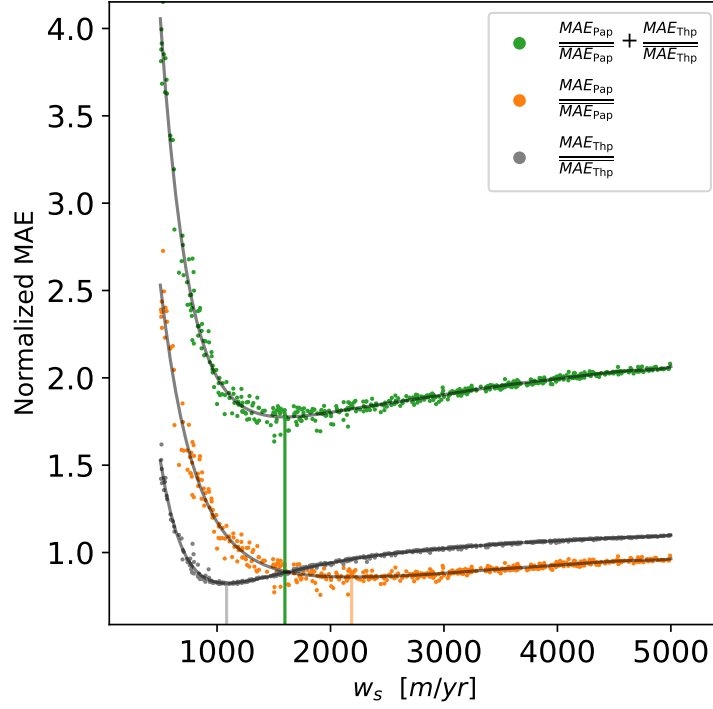


**Figure 4.** Particle-bound Mean Absolute Error (MAE) score functions (normalised according to Eq. (12)) as a function of sinking speed  $w_s$ . Every dot represents a model simulation of the 511-member ensemble that varies all parameters ( $w_s, k_{des}^j, \sigma_i^j$ ). Solid lines are fitted polynomials of degree 10. Shown are the Pa<sub>p</sub> and Th<sub>p</sub> terms of Eq. (12) and their total (green). The vertical green line indicates the minimum of the total, which yields the best value:  $w_s = 1600$  m/yr.

**Table 4.** Main model runs in this study. Additional runs are given in Table C1. All simulations were run into steady state for 5,000 years. All runs have the same parameter settings, dust and nepheloid particles as CTRL, unless indicated otherwise. Biological particles comprise POC,  $\text{CaCO}_3$  and opal.

Runname	AMOC	Forcing <sup>a</sup>	Biological particles <sup>b</sup>	Description
CTRL	17.8 Sv	-	dyn.	Tuning result; CTRL=Pdyn_18Sv
Pdyn_14Sv	13.9 Sv	0.10	dyn.	Weaker AMOC ( $\sim 14$ Sv)
Pdyn_11Sv	11.2 Sv	0.15	dyn.	Weaker AMOC ( $\sim 11$ Sv)
Pdyn_9Sv	8.6 Sv	0.20	dyn.	Weaker AMOC ( $\sim 9$ Sv)
Px1_18Sv	17.8 Sv	-	fixed ( $\times 1$ )	CTRL with fixed particles
Px1_14Sv	13.9 Sv	0.10	fixed ( $\times 1$ )	$\sim 14$ Sv AMOC with fixed particles
Px1_11Sv	11.2 Sv	0.15	fixed ( $\times 1$ )	$\sim 11$ Sv AMOC with fixed particles
Px1_9Sv	8.6 Sv	0.20	fixed ( $\times 1$ )	$\sim 9$ Sv AMOC with fixed particles
NO_NEPH	17.8 Sv	-	dyn.	No neph ( $\sigma_{ne}^j = 0$ )
NO_DUST	17.8 Sv	-	dyn.	No dust ( $\sigma_{du}^j = 0$ )
NO_REM	17.8 Sv	-	dyn.	No remineralisation term

<sup>a</sup>Freshwater forcing [Sv] in the North Atlantic between  $45^\circ\text{N}$  and  $70^\circ\text{N}$ .

<sup>b</sup>Dynamically simulated (dyn.) or fixed to yearly avg. particles from CTRL ( $\times$  a factor 1).

(full compilation in Supplementary Dataset S3). Levier et al. (2022) was published after our tuning so is not included in this compilation. Their study estimates a value of  $K_{op}^{\text{Pa}}$  similar to Chase et al. (2002), thus not changing our results. The 3000 runs were performed with all  $\sigma_i^j$  taken randomly ranging from the minimum of observations to twice the maximum of observations using Latin hypercube sampling. We picked the  $\sigma_i^{\text{Pa}}$  values from the run that a) is within the 10 runs giving the best  $MAE_{\text{Paad}}$  score, and b) has the best  $MAE_{\text{Pap}}$  out of those 10 runs; analogously for Th (Supplementary Fig. S3).

## 2.6 Model simulations

Three types of runs were performed: runs for tuning (see Sect. 2.5), runs at pre-industrial (PI) steady state (e.g., CTRL; results in Sect. 3.1) and runs with adjusted AMOC and/or particles (results in Sect. 3.2). The most relevant model runs discussed in this study are listed in Table 4; additional experiments are in Table C1.

The default Bern3D spinup procedure is used to establish a steady state at pre-industrial conditions with  $\text{CO}_2=278$  ppm and orbital conditions corresponding to 1765 CE, where the simulated ocean circulation is in equilibrium with the atmospheric energy-moisture balance module, and biogeochemical tracers (such as the nutrients needed for POC and opal) established their distribution throughout the ocean during 10,000 simulation years. The resulting AMOC maximum is 17.8 Sv and particle fields are simulated as shown in Fig. 2. All simulations start from this steady state and run for 5,000 simulation years, except weak AMOC runs (see below).

The runs at pre-industrial steady state are: CTRL, NO\_NEPH, NO\_DUST and NO\_REM. The control run (CTRL) contains the best-fit ( $w_s$ ,  $k_{des}^j$ ,  $\sigma_i^j$ ) result from the tuning. To examine the impact of our new model development, we perform three sensitivity runs: without nepheloid layers (NO\_NEPH), without dust (NO\_DUST) and without the remineralisation term (NO\_REM).

In model experiments called Pdyn\_, Px\_ and P/\_, the AMOC and/or particle export fields are adjusted simultaneously. The AMOC is adjusted by applying a constant freshwater flux to a part of the North Atlantic.

In experiments with varying particles (Pdyn), changes in ocean circulation directly affect biological particle concentrations. This setup is used in the CTRL, Pdyn\_14Sv, Pdyn\_11Sv and Pdyn\_9Sv runs, whereas for runs with prefixes Px1\_ and P/2\_, Px2\_ Px3\_, and Px5\_ (listed in Table C1) biological particle export fields are fixed to the yearly average of the particle fields obtained from the CTRL simulation (scaled by a factor). Although changes in the particle export pattern can change Pa/Th, we choose to keep the pattern constant (only scaling the export) due to a lack of reliable reconstructions of past particle export.

To generate weakened AMOC states, we apply a continuous freshwater forcing to the North Atlantic (45°N-70°N). The total freshwater amount is compensated for by a salt flux distributed over the rest of the surface ocean cells to avoid salt feedbacks elsewhere (Stocker et al., 2007). Freshwater forcings of 0.10, 0.15 and 0.20 Sv are applied, resulting in steady state AMOC strengths of 13.9, 11.2 and 8.6 Sv (78 %, 63 % and 48 % of the CTRL AMOC). Steady states with an AMOC weaker than 8.0 Sv are unfortunately not stable in the Bern3D model, as the addition of more freshwater causes a new steady state with a collapsed AMOC. The weakened AMOC state runs are run into equilibrium for 5,000 years and then used as starting points for the \_14Sv, \_11Sv and \_9Sv Pa-Th simulations (AMOC strengths are rounded in the suffixes), during which the freshwater forcings are still applied continuously.

### 3 Results and discussion

#### 3.1 Model tuning and comparison to modern data

Our multi-step tuning of simulated Pa and Th to modern seawater data provides important constraints. Figure 4 shows the result and the separate terms of the particle sinking velocity. Fitted polynomials were used to avoid dominance by outliers. Larger  $w_s$  cause lower average  $\text{Pa}_p$  and  $\text{Th}_p$  because both particle-bound isotopes are removed more quickly by sinking particles. Hence, for large  $w_s$ , MAEs approach an upper limit corresponding to the removal of virtually all  $\text{Pa}_p$  and  $\text{Th}_p$  ( $\text{sim}_l = 0$  in Eq. (11)). The sinking speed minimising the model-data difference of  $\text{Th}_p$  (grey) is 1084 m/yr and is much lower than that of  $\text{Pa}_p$  (orange), which is 2186 m/yr. This is because Th has a higher affinity to smaller particles than Pa has (Kretschmer et al., 2011). Smaller particles are parts of POC, dust and possibly nepheloid-layer particles. These smaller particles sink



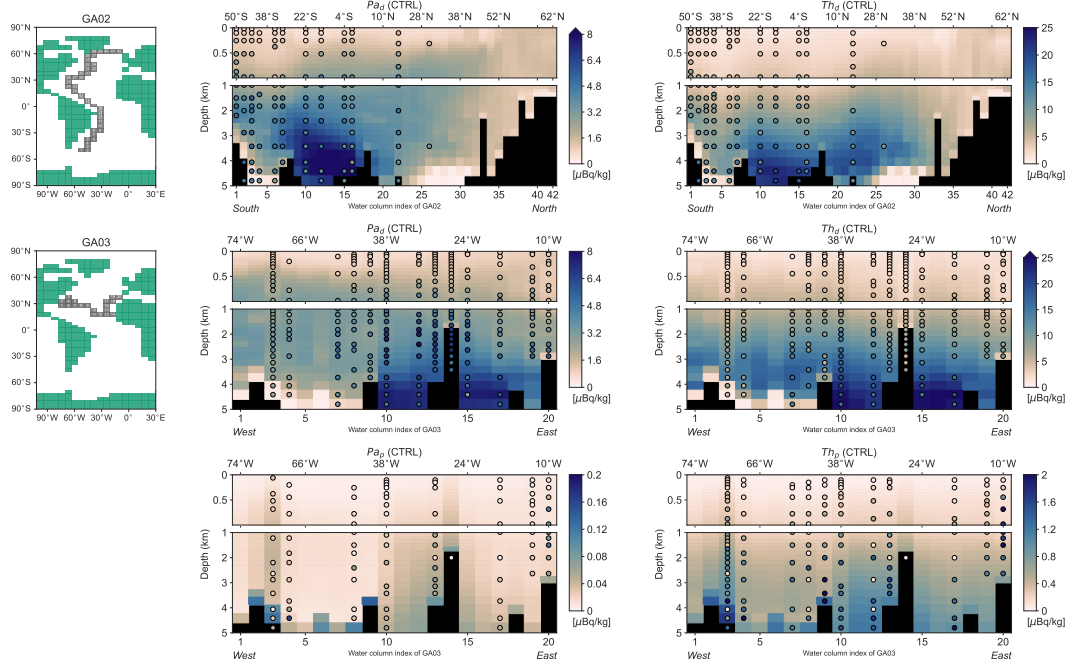


**Figure 5.** CTRL model output (background) with seawater observations (circles) along two large transects in the Atlantic for  $Pa_d$ ,  $Th_d$ ,  $Pa_p$  and  $Th_p$  (where available). Data references in Sect. 2.3. Numbering on the transect maps (left) defines the order of plotting and corresponds to the water column indices on the  $x$ -axis of that transect. Seawater data circles are plotted centred in the nearest model grid cell box. If a grid cell contains multiple seawater observations, an uncertainty-weighted average is taken.

slower such that the best-fit average sinking speed for  $Th$  is lower than for  $Pa$ . The minimum of the combined cost function (green line) lies at  $w_s = 1600$  m/yr.

For the desorption constants, we only evaluate  $MAE_{Pa_d}$  and  $MAE_{Th_d}$ , because  $MAE_{Pa_p}$  and  $MAE_{Th_p}$  have very low sensitivity to  $k_{des}^j$  (not shown). The optimal  $k_{des}^j$  lie between 3.5 and 4.5/yr and depend on the parameter set (Supplementary Fig. S2). We conclude that  $k_{des}^{Pa}$  and  $k_{des}^{Th}$  are not significantly different and we take  $k_{des}^j = 4.0$ /yr as best value for both elements  $j$ . The last tuning step is described in Supplementary Text S2 and Supplementary Fig. S3. The resulting tuned  $\sigma_i^j$  values are denoted in Table 3 as “This study (CTRL)”.

Figure 5 shows the CTRL run output of annual average  $Pa_d$ ,  $Th_d$ ,  $Pa_p$  and  $Th_p$  together with seawater observations along two major Atlantic GEOTRACES transects, GA02 and GA03. Note that these transects were also part of the tuning dataset. Figure C1 shows the same for more Atlantic transects (Deng et al. (2018), GA10, GIPY04 and GIPY05). Dissolved concentrations start out low in the northern North Atlantic along the GEOVIDE transect (Deng et al., 2018), both in the modelled CTRL and observations, as expected for newly formed deep waters, because these waters were near the surface recently and therefore could only accumulate low concentrations. CTRL  $Pa_d$  and

Th<sub>d</sub> fit reasonably well with observations along the meridional transect GA02, and clearly show higher concentrations in the south, which originate from the accumulation of Pa and (less so) Th transport time. The CTRL, however, overestimates South Atlantic Pa<sub>d</sub> and Th<sub>d</sub> compared to GA02 measurements and possibly simulates the maximum not far south enough. The effect of bottom scavenging is apparent in the low Pa<sub>d</sub> and Th<sub>d</sub> around the Bermuda Rise region and in the Argentinian basin. The other major transect GA03, traversing the North Atlantic from west to east, shows a better fit with a gradient towards higher Pa<sub>d</sub> and Th<sub>d</sub> values in the east, both modelled and observed. This concentration gradient between deep western and eastern boundary currents is resolved in the Bern3D model simulations. Along GA03, simulated Pa<sub>p</sub> agrees reasonably well with observations, but Th<sub>p</sub> is too low in the model by on average 47 %. In the Southern Ocean (GIPY04 and GIPY05 in Fig. C1) modelled values are too low everywhere: on average 48 % too low for Pa<sub>d</sub> and Th<sub>d</sub>, 61 % for Pa<sub>p</sub> and 72 % for Th<sub>p</sub>. For Th<sub>p</sub> we also recognise too little variation with depth here. This is probably caused by a too narrow Southern Ocean opal belt in the model (Fig. 2c), which should extend southwards towards the Antarctic coast (Sarmiento & Gruber, 2006). A second cause is a too strong modelled impact of nepheloid layers (discussed below).

We conclude that the high values of Pa<sub>d</sub> and Th<sub>d</sub> simulated in the West Atlantic (GA02) up to ca. 30°S are consistent with the data but should extend all the way southwards according to observations. This could be caused by a too strong modelled impact of nepheloid layers around the Argentinian basin and Southern Ocean or by a too weak AABW circulation in the model compared to observations.

Next, we assess modelled Pa<sub>p</sub>/Th<sub>p</sub> ratios and compare them with Holocene sediments, which were not used for the tuning. Overall, the agreement between simulated (ocean-floor) and sedimentary Pa<sub>p</sub>/Th<sub>p</sub> is very good (Fig. 6). Depths between model and sediment cores can differ because the model has average water column depths, whereas sediment cores follow local bathymetry. This discrepancy explains the two outliers in the West Atlantic at 10°N and 15°N, where the shallower sediment cores were located at a fracture zone and on a seamount (Ng et al. (2020): cores 56 and 57 (on top of each other in Fig. 6) and core 46. The low values in Fig. 6 illustrate that Pa is exported out of the open Atlantic relative to Th (blue; Pa/Th below production ratio) towards the Southern Ocean (red; Pa/Th above production ratio). The continental margins and the northern opal belt also experience an import of Pa relative to Th because of abundant particles.

Now we examine the impact of our new model development concerning nepheloid layers, dust particles, and element release during remineralisation. The addition of benthic nepheloid layers largely improved Pa<sub>d</sub> and Pa<sub>p</sub>/Th<sub>p</sub> in the Atlantic (Supplementary Fig. S5): the MAE metric compared to modern seawater data improved from 1.5 in NO-NEPH to 1.0  $\mu\text{Bq s}^{-1}$  in CTRL for Pa<sub>d</sub> and from 0.044 to 0.030  $\mu\text{Bq s}^{-1}$  for Pa<sub>p</sub>/Th<sub>p</sub>. However, for Atlantic Th<sub>d</sub> MAEs slightly increased from 1.9 to 2.1  $\mu\text{Bq s}^{-1}$ , indicating a marginally worse fit. Since the tuning was performed over all ocean basins, regional

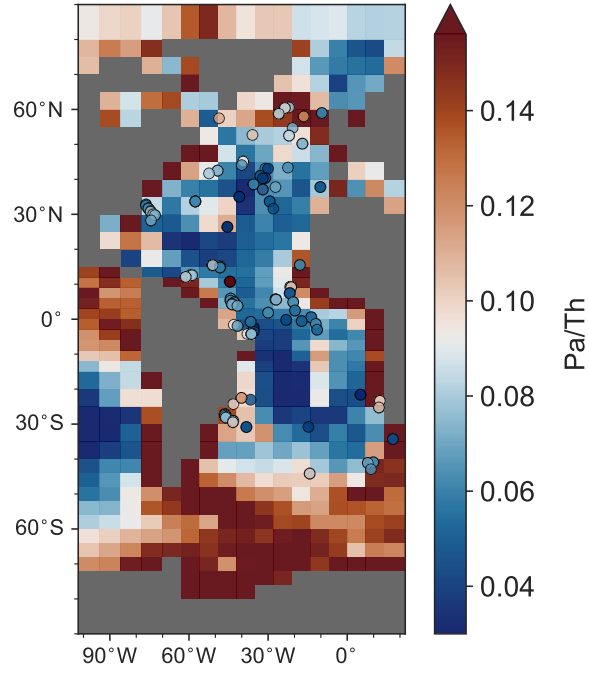


**Figure 6.** Sedimentary Pa/Th. Background coloured squares:  $\text{Pa}_p/\text{Th}_p$  ratio in the bottom ocean grid cells for the CTRL simulation. Circles: sediment Holocene core-top  $\text{Pa}_p/\text{Th}_p$  measurements (Holocene average) from Fig. 3a/Table 2. Values lower (higher) than the production ratio of 0.093 are blue (red) indicating Pa export from (import to) that water column. If sediment cores are located close to each other, circles may fall behind other circles.

differences exist, such that the CTRL results are not always better than NO\_NEPH, NO\_DUST and NO\_REM in all basins and for all  $A_i^j$  simultaneously. The improvement of adding nepheloid layers in the Atlantic and Pacific comes at the cost of too low  $\text{Pa}_d$  and  $\text{Th}_d$  in the Southern Ocean, where NO\_NEPH performs better than CTRL. This indicates a too strong impact of nepheloid layers in the Southern Ocean. In this region we filled nepheloid-layer data gaps with high values, which is confirmed by a recent study of eddy kinetic energy (Ni et al., 2023) implying strong nepheloid layers in the Southern Ocean (Gardner et al., 2018b). Even though our nepheloid-layer maps (Fig. 2e-f) seem correct, it is plausible that the modelled impact of nepheloid layers is still too strong via too high values of  $\sigma_{ne}^j$  (recall that the tuning was not sensitive to  $\sigma_{ne}^{Pa}$ ). In contrast, dust and the remineralisation term played a smaller role than nepheloid layers. Adding dust improved the match with seawater data in the regions of the Saharan and South American dust plumes, leading to a small change in overall Atlantic MAEs (Supplementary Fig. S6). The newly added remineralisation term only had a small effect, which is hardly discernible (Supplementary Fig. S7). This is because below 600 m the vertically uniform desorption process dominates over remineralisation, which decreases exponentially with depth. To conclude, these sensitivity tests emphasise that the potential impact of nepheloid layers in model simulations is large everywhere, and adding scavenging dust particles helps to find the right balance in regions where dust plumes are prevalent.

We also tested the effect of a benthic flux of  $^{231}\text{Pa}$  and  $^{230}\text{Th}$  coming out of the sediment. Opal particles remineralise slowly, and most opal that reaches the deep sediment still dissolves when in the sediment (Abrantes, 2000), from where opal can release opal-bound Pa or Th again into the pore water as dissolved Pa or Th. This could potentially affect the Pa/Th budget in the deep ocean, and was so far not considered in models. We simulated 20 % of the opal-bound Pa and/or Th as a source of dissolved Pa or Th at the bottom-most grid cells. However, this made no visible difference such that we decided not to include this process in the model.

### 3.2 Detectability of the AMOC signal in sedimentary Pa/Th

To assess the influence of AMOC strength on sedimentary Pa/Th, we use two measures: ‘detectability’, represented by how well Pa/Th can detect Pa export out of the North Atlantic (described in this section’s Fig. 8), and ‘sensitivity’, the response of Pa/Th to AMOC change (described in Fig. 11). Thus, detectability is a measure of the direct impact NADW advection has on Pa/Th based on the initial interpretation of the Pa/Th proxy, whereas the sensitivity is a result of changes in both AMOC and particle fluxes.

We first investigate the basin-scale AMOC detectability of Pa/Th by assessing the budget of protactinium and thorium in the North and South Atlantic. Here, we follow the approach of Deng et al. (2018), who computed meridional import and export fluxes of Pa and Th of the North and South Atlantic basins based on modern observations (Fig. 7a). Deng et al. (2018) estimated that today 26 % of the Pa produced in the North Atlantic is exported out of it but only 4 % of Th (Fig. 7a). The authors interpreted the

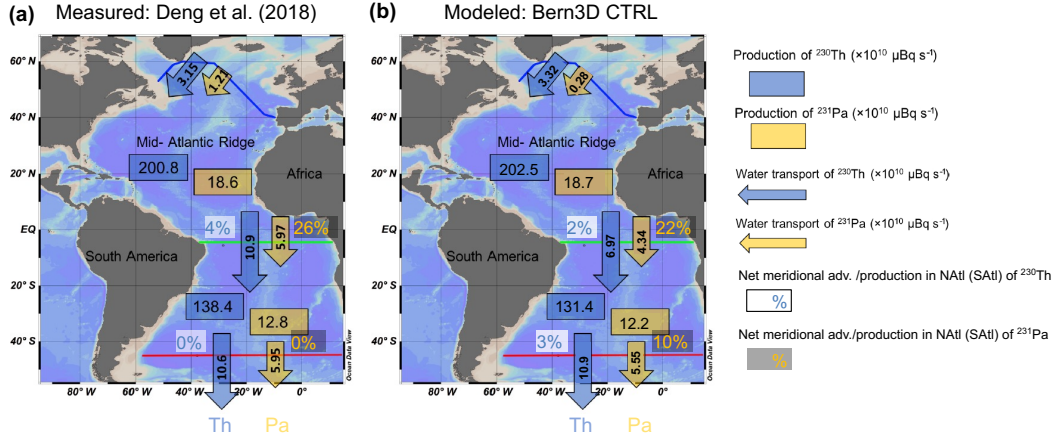


**Figure 7.** Budget of Atlantic Pa (yellow) and Th (blue) in  $\mu\text{Bq s}^{-1}$  as computed **a)** from measurements by Deng et al. (2018) and **b)** from the Bern3D model CTRL run. Boundaries of the North and South Atlantic follow the transects GEOVIDE, WOCE A07 (4.5°S), and WOCE A11 (simplified version shown) (Deng et al. (2014); see Fig. C2 for the transects on the Bern3D grid). Percentages express how much of the produced Pa and Th is exported out of the North respectively South Atlantic sub-basin by advection. The rest either sinks to the sediment within the sub-basin or is transported out of it by horizontal diffusion of Pa and Th. Adapted from Deng et al. (2018).

ca. 22 percent points difference between North Atlantic Pa and Th export to be caused by the meridional transport of Pa along NADW. For the South Atlantic the authors found no net import or export for both isotopes. After entering the Southern Ocean, most of Pa finds its final sink in the Southern Ocean opal belt.

We perform the same budget analysis as Deng et al. (2018), now based on variables diagnosed from the Bern3D CTRL run (Fig. 7b). The three transects were converted to the Bern3D grid (Fig. C2) and their throughflows were computed similarly by diagnosing the horizontal velocities flowing through the section by using the adjacent  $\text{Pa}_d$ ,  $\text{Th}_d$  concentrations from the CTRL run (results in Supplementary Table S1). Fluxes into the Mediterranean Sea were also computed but are negligible ( $< 0.02 \times 10^{10} \mu\text{Bq/s}$ ). Overall, net results in the North Atlantic are similar between the Bern3D model and Deng et al. (2018): we find that 22 % of Pa produced in the North Atlantic is exported southward but only 2 % of Th. This agreement (26 % Pa and 4 % by Deng et al. (2018)) builds trust in the Bern3D model's large-scale circulation and implementation of protactinium-thorium. In the South Atlantic however, we find that 10 % of Pa is advected further southward, whereas Deng et al. (2018) measured a net 0 %. This net transport out of the South Atlantic results from a combination of southward transport in the west and northward transport in the east, where the latter is impacted by too low Southern Ocean  $\text{Pa}_d$  and  $\text{Th}_d$  concentrations in the Bern3D model compared to seawater observations (see Fig. C1, top row) thereby impacting the net result.

	AMOC strength			
	8.6 Sv	11.2 Sv	13.9 Sv	17.8 Sv
Dynamic particles -	5.9%	10.3%	15.1%	20.0%
PI particles /2 -	4.5%	8.7%	14.9%	22.7%
PI particles x1 -	3.8%	7.9%	14.0%	20.0%
PI particles x2 -	2.2%	5.4%	10.1%	12.4%
PI particles x3 -	1.4%	3.9%	7.4%	8.1%
PI particles x5 -	0.6%	2.2%	4.3%	4.3%

**Figure 8.** Heat map of NATl (North Atlantic) Pa export [%] minus NATl Th export [%], which is a measure for the detectability of NATl Pa export in Pa/Th: green if NATl Pa export is detectable and beige if it is not detectable. A detectability threshold of 5 percent point is assumed, indicated by the black boundary. Simulations with varying AMOC (x-axis) and varying particles (y-axis) were used (Tables 4 and C1). The first row indicates runs where particles dynamically adjust to ocean circulation, whereas next rows keep particle export patterns fixed to the pre-industrial (PI) CTRL and scale the amount.

While we draw no conclusions about the South Atlantic because of the model-observations discrepancy there, our findings confirm that present-day deep ocean circulation significantly fractionates Pa and Th in the North Atlantic. This clear difference between Pa and Th export out of the North Atlantic at present-day makes the AMOC strength detectable at a sub-basin scale. Averaging enough measurements of North Atlantic sedimentary Pa/Th, to ensure that local conditions do not dominate, will reflect this sub-basin export caused by NADW advection.

But are other AMOC states detectable as well? We further investigate the detectability under varying conditions using idealised model experiments with weakened AMOC and/or strengthened particle productivity. These experiments are sensitivity tests to understand the proxy's response to (extremely) different conditions. For instance LGM conditions are expected to lie within these AMOC and particle scaling boundaries (Lynch-Stieglitz et al., 2007; Schmiedl & Mackensen, 1997; Abrantes, 2000; Wollenburg et al., 2004; Mahowald et al., 2006). We choose the modelled percent point difference between North Atlantic Pa and Th export (20 percent points in CTRL) as a measure for the detectability of the AMOC signal in Pa/Th and compute this percent point difference for all runs with varying AMOC strength and particle concentrations. If this percentage difference is not significantly different from 0 % (choosing <5 %), we assume that the AMOC-signal is not detectable anymore in Pa/Th for that state.

The resulting percentage differences are shown in the first row of Fig. 8 for runs with varying AMOC and particles simulated dynamically (runs Pdyn\_9Sv, Pdyn\_11Sv,

Pdyn\_14Sv and CTRL). The top right value of 20.0 % corresponds to Fig. 7b of the CTRL run, with 22 % North Atlantic Pa export minus 2 % North Atlantic Th export. The following rows (row 2-6) contain results from runs with varying AMOC and fixed biological particles. Depending on the row, particle exports are fixed to their CTRL state scaled by a factor of 0.5, 1, 2, 3 or 5 (runs are listed in Table C1). This way we vary AMOC (columns) and particle concentrations (rows) independently. The subtracted North Atlantic Th export is usually smaller than 2 %, except for run P/2\_18Sv with 5.5 % due to low particle fluxes. We conclude that even a weak AMOC of 8.6 Sv can still be detected by North Atlantic Pa/Th for runs with dynamical particles. However, if biological particles are fixed (i.e., independent from the AMOC in the model) to their pre-industrial distributions (PI particles  $\times 1$ ), an 8.6 Sv AMOC is not detectable (a stronger AMOC of 11.2 Sv is).

When comparing rows 1 and 3 of Fig. 8, it is evident that the AMOC signal is better detectable if particles are dynamically simulated (i.e., they respond to the AMOC change). The main reason for this is that a weaker AMOC also reduces the transport of nutrients back to the 40-60°N surface ocean, both via lessened lateral transport and via increased stratification, which reduces the mixing of surface waters with nutrient-rich deep waters (Schmittner, 2005). Therefore, this region becomes more limited by phosphate availability and export productivity decreases (Fig. C3-C4) (Nielsen et al., 2019). These lower particle concentrations result in lower  $\text{Pa}_p$  hence  $\text{Pa}_p/\text{Th}_p$  in region 1 (the northern North Atlantic) in runs Pdyn\_9Sv, Pdyn\_11Sv and Pdyn\_14Sv compared to CTRL. Equivalently, more  $\text{Pa}_d$  is kept available for southward advection and this makes the NADW strength better detectable than if particles would not respond to the AMOC change.

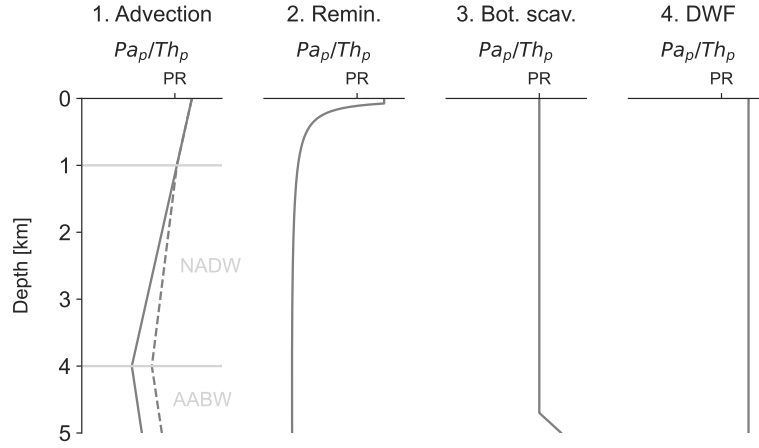
Thus, the effects associated with dynamical changes in particle concentrations enhance the signal from NADW advection on Pa/Th – two processes that are generally assumed to partly cancel each other. For fixed particle patterns, AMOC detectability is not significantly different if the amount of particles is reduced by a factor of 2 higher or lower (compare rows 2-4 of Fig. 8). Under a stronger particle increase with a factor of 3, the 11.2 Sv AMOC is not detectable anymore, and with particle concentrations multiplied by a factor 5 even the present-day AMOC state would not be detectable by North Atlantic Pa/Th. In other words, for these experiments the particle effect completely dominates over the advection signal, comparable to the modern situation in the more stagnant Pacific.

### 3.3 Reasons for correlation and anti-correlation of Pa/Th with AMOC

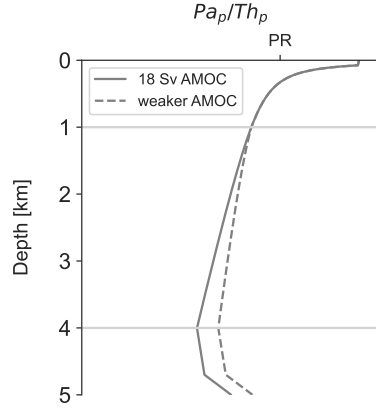
Depth profiles of Pa/Th are not straightforward to interpret in terms of AMOC strength. They are primarily a function of the prevailing advection, particle flux regime, remineralisation and history of the water mass. In the following, we classify which regions and depth ranges exhibit a positive correlation of Pa/Th with AMOC strength (called correlation here) or a negative correlation (anti-correlation; as observed at the Bermuda Rise; e.g., McManus et al. (2004)), and to understand the reasons responsible for this



**(a)** Processes forming Atlantic  $Pa_p/Th_p$  profiles (in the presence of rev. scav.)



**(b)** Atl. 35°S-35°N (process 1-3)



**(c)** Atl. 40-70°N (process 2-4)

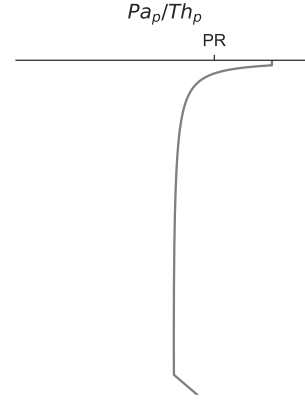


**Figure 9.** **a)** Impact of different processes on  $Pa_p/Th_p(z)$  (in the presence of reversible scavenging to sinking particles): 1. Advection; 2. Production and remineralisation of particles; 3. Bottom scavenging; 4. Deep Water Formation. PR stands for the production ratio. Typical profiles follow by combining **b)** processes 1-3 for the mid-latitude and equatorial Atlantic, and **c)** processes 2-4 for the North Atlantic DWF region.

behaviour through model experiments. We start by examining different influencing factors on  $Pa/Th$  depth profiles as expected from theory.

The theoretical impact of different processes on Atlantic  $Pa_p/Th_p(z)$  is sketched in Fig. 9a, where the process of reversible scavenging to sinking particles is always applied; without reversible scavenging, processes 1-4 would not alter  $Pa/Th$ . Reversible scavenging with a constant particle sinking flux leads to linear depth profiles  $A_p^j(z) = \frac{\beta^j}{w_s} z$  in the absence of circulation (Bacon & Anderson, 1982). Remote from areas of boundary scavenging and without considering diffusive transport (Hayes et al., 2015a), the process of reversible scavenging to sinking particles thus gives a  $Pa/Th$  ratio equal to the production ratio:  $Pa_p/Th_p(z) = \frac{\beta^{Pa}}{\beta^{Th}} = 0.093$ , which serves as a starting point. Hori-



zontal advection by NADW decreases Pa/Th in the mid-latitude and equatorial Atlantic, because NADW transports  $\text{Pa}_d$  away (process 1) (Burckel et al., 2016). Under a weaker AMOC (dashed line), the slope changes with NADW having less impact. Below ca. 4 km depth, AABW (Antarctic bottom water) brings in water with a higher Pa/Th coming from the south. In process 2, particle concentrations are high at the surface and decrease with depth below the euphotic zone due to remineralisation. In the Atlantic CTRL run (excluding the southern opal belt), the scavenging behaviour of Pa is clearly dominated by POC while Th is dominated by  $\text{CaCO}_3$ , so we approximated the impact of remineralisation on Pa/Th( $z$ ) by drawing  $R_{\text{POC}}(z)/R_{\text{Ca}}(z)$ . Bottom scavenging increases Pa/Th values in the nepheloid layer because the fractionation between Pa and Th diminishes here. In practice, the effects of bottom scavenging and AABW advection are difficult to distinguish. Process 4, deep water formation, occurs in the northern North Atlantic and transports high Pa/Th ratios from the surface downward (assuming 100 % of the water sinks in this idealised water column).

Typical Pa/Th depth profiles of the mid-latitude and equatorial Atlantic in Fig. 9b result from combining these individual processes. A weaker AMOC advection shifts Pa/Th to higher values, highlighting the negative correlation (anti-correlation) between Pa/Th and AMOC strength, as expected from the basic concept of the proxy. Different regions have different surface values, depending on local water mass history and the concentrations and composition of particles. Since dissolved concentrations at the surface are low, while particle flux is high, the shallow Pa/Th budget can be overprinted by imported Pa. The deepest parts of the profiles depend on the height and intensity of the benthic nepheloid layers (recall Fig. 2e-f). For the North Atlantic deep water formation (DWF) region (Fig. 9c), process 1 (advection) is omitted and replaced by process 4 (DWF), resulting in a steeper downward signal.

Now we move from this idealised sketch to the model outputs (Fig. 10), where four regions of interest are chosen in the West Atlantic, where sufficient sedimentary Pa/Th observations are available (Fig. 3b). These regions lie in the northern North Atlantic and at different latitudes of the West Atlantic. We focus on the West Atlantic in regions 2-4, since the strong western and deep western boundary currents result in a higher signal-to-noise ratio in Pa/Th. We first consider region 1, a wider region in the northern North Atlantic, which covers the southern edge of the region where NADW formation takes place in the model, but also contains parts where NADW already undergoes horizontal advection. For fixed particle fields (panel a), weaker AMOC runs show higher Pa/Th at depth, resulting in an anti-correlation between Pa/Th and AMOC in region 1 (the northern North Atlantic). In contrast, the more realistic runs with dynamically simulated biological particles (panel b) result in a correlation instead, which agrees fairly well with available sediment measurements (Süfke et al., 2020; Gherardi et al., 2009). As discussed before, under AMOC weakening less particles are present in region 1 (the northern North Atlantic), leading to lower surface Pa/Th in Fig. 10b compared to Fig. 10a. These changes at the surface result in a shift of the weaker-AMOC profiles towards the left of the CTRL.

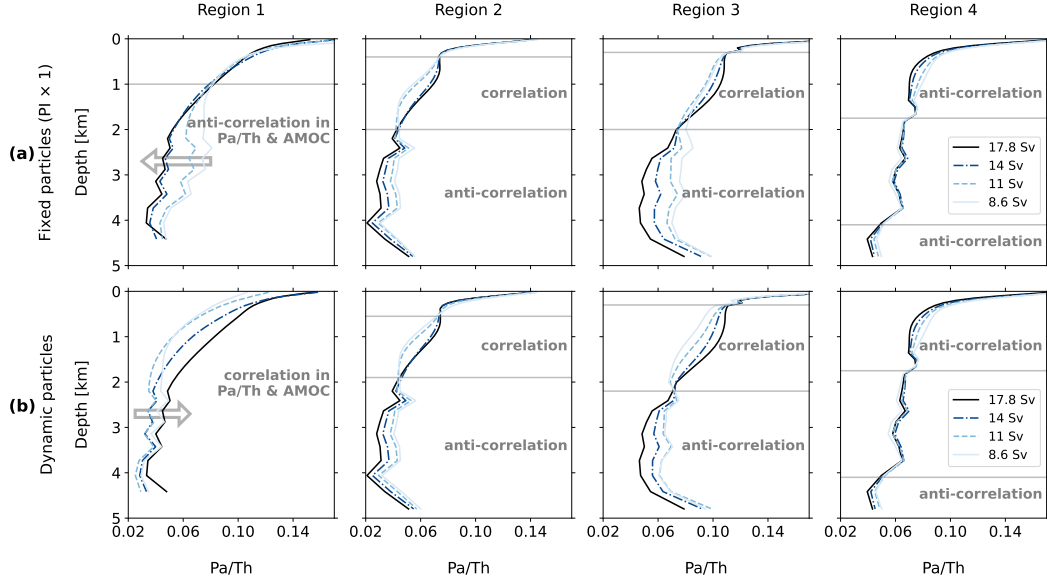


**Figure 10.** Modelled depth profiles of  $\text{Pa}_p/\text{Th}_p$  in four regions of the West Atlantic, from north (region 1) to south (region 4; Fig. 3b). **a)** Runs Px1\_18Sv, Px1\_14Sv, Px1\_11Sv and Px1\_9Sv with varying AMOC and particles fixed at the pre-industrial (PI) control. **b)** Runs CTRL, Pdyn\_14Sv, Pdyn\_11Sv and Pdyn\_9Sv with varying AMOC and dynamically simulated particles, which adjust to changes in ocean circulation and nutrients redistribution, yielding more realistic simulation results. Arrows point in the direction of increasing modelled AMOC strength. Annotated text and grey lines demarcate domains with a recognisable anti-correlation between  $\text{Pa}/\text{Th}$  and AMOC (arrow to left; black line left of blue lines) respectively a correlation (arrow to right; black line right of blue lines).

At the low- to mid-latitude regions 2-4, Pa/Th depth profiles are influenced strongly by advection. The response of biological particles to AMOC change is smaller in these regions such that their depth profiles in Fig. 10a resemble Fig. 10b. When moving southward from region 2 to region 4, the absolute Pa/Th values in the CTRL run steadily increase at 2-4 km because we travel meridionally along with NADW advection, with  $\text{Pa}_d$  thus  $\text{Pa}_p$  continuously accumulating. Pa/Th is especially low in region 2 (the Bermuda Rise region) because of abundant particles here. In the upper 2 km we find more processes at play than in Fig. 9b, which result in a correlation in regions 2-3 (ignoring the surface layer) and an anti-correlation in region 4. Namely, in regions 2 and 3, the upper 2 km of the water column behaves opposite to the deeper ocean in its Pa/Th response to AMOC strength. This is because the upper 2 km in the model are still governed by the upper limb of the AMOC, which transports water northwards and brings extra  $\text{Pa}_d$  to the North Atlantic when the AMOC is strong (Gu & Liu, 2017). Below 2 km, regions 2 (the Bermuda Rise region) and 3 (the equatorial West Atlantic) exhibit an anti-correlation as expected (Fig. 9b), whereas region 4 (the Southwest Atlantic) has no detectable AMOC-dependent signal at these water depths, presumably due to the cancelling effects of changes in Pa import and Pa export here. Region 3 (the equatorial West Atlantic) is somewhat more sensitive to AMOC changes at depth than region 2 (the Bermuda Rise), especially to an AMOC decrease from 18 to 14 Sv. Therefore, we propose that equatorial West Atlantic Pa/Th deserves as much attention as Bermuda Rise Pa/Th, with the advantage of a smaller contribution of bottom scavenging.

The sensitivity of  $\text{Pa}_p/\text{Th}_p$  to a reduced AMOC is summarised in Fig. 11 along the Atlantic GEOTRACES transects GA02 and GA03. In red (blue) regions, the 9 Sv run has higher (lower) Pa/Th than the 18 Sv run, corresponding to a negative (positive) correlation between Pa/Th and AMOC. Local strong bottom scavenging causes high values in a few bottom water grid cells. The GA03 transect shows that east-west differences are minor, except close to the West African coast, where particles are highly abundant. As in Fig. 10, the most striking particle-response along GA02 is visible at 40-60°N (region 1), which is the region with the strongest change in particle concentrations. The strong negative anomaly at 40-55°N for dynamic particles is a result of the reduced export productivity there in  $\text{P}_{\text{dyn}}9\text{Sv}$ : particle concentrations of POC,  $\text{CaCO}_3$  and especially biogenic opal are reduced (virtually no northern opal belt is present anymore). This causes a large change in Pa/Th compared to CTRL at the northern opal belt location. The weak correlation (light blue) throughout the South Atlantic is caused by the South Atlantic being the constant destination of Pa imported from the north. Namely, the CTRL AMOC state produces a small but discernible gradient in  $\text{Pa}_p/\text{Th}_p$  from north to south in the deep ocean (in absence of local particle effects; see Fig. 5). A weaker AMOC state advects less  $\text{Pa}_d$  such that this gradient lessens. In other words, under AMOC weakening, more  $\text{Pa}_d$  stays in the region of origin (increasing Pa/Th in the North Atlantic hence an anti-correlation) and less additional  $\text{Pa}_d$  arrives in the South Atlantic (decreasing Pa/Th, hence a correlation). The darkest colours in Fig. 11 (top right panel) indicate the latitudes and depths most promising for the Pa/Th proxy - although east-west

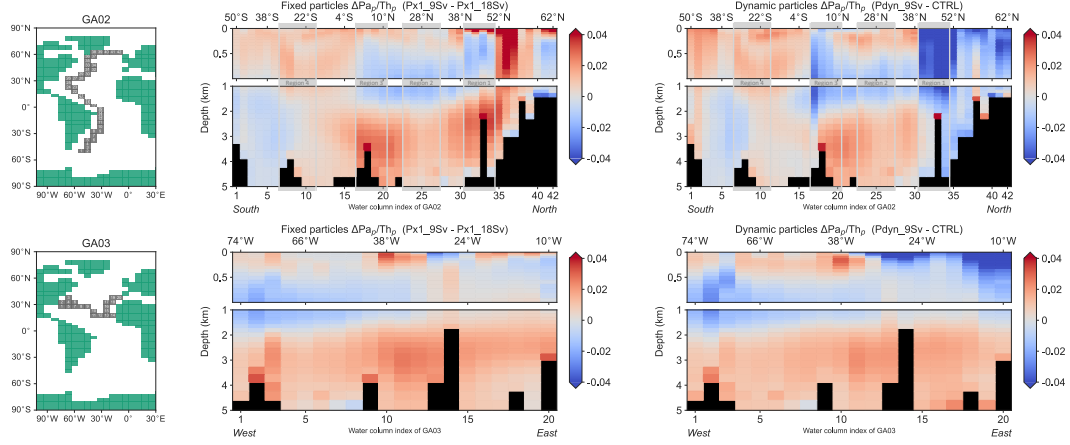


**Figure 11.** Sensitivity of modelled  $\text{Pa}_p/\text{Th}_p$  to a  $\sim 50\%$  AMOC weakening along the two major Atlantic transects. Red indicates increasing  $\text{Pa}/\text{Th}$  when AMOC decreases, and blue indicates decreasing  $\text{Pa}/\text{Th}$  when AMOC decreases. The result is shown for fixed particles (PI particles  $\times 1$ ) in the middle panels by subtracting run's  $\text{Px1.18Sv}$   $\text{Pa}_p/\text{Th}_p$  from that in  $\text{Px1.9Sv}$ , and for dynamic particles in the right panels, where  $\text{CTRL} = \text{Pdyn.18Sv}$ .

differences may still exist. This reveals that additional sediment cores in the shallower 40-60°N, between 1 and 2 km depth, could be very promising. The few existing down-core  $\text{Pa}/\text{Th}$  profiles in this region often record large changes in opal between Holocene and LGM such that their  $\text{Pa}/\text{Th}$  has not been used to infer AMOC signals until now. The way how opal, POC and  $\text{CaCO}_3$  particles respond to a weaker AMOC enables us to reconstruct AMOC changes with  $\text{Pa}/\text{Th}$  in a different way in this region. However more modelling studies investigating this effect would be beneficial in order to assess the reliability of the particle response in the Bern3D model.

Previous modelling studies also assessed the sensitivity of sedimentary  $\text{Pa}/\text{Th}$  to variations in AMOC (Marchal et al., 2000; Gu & Liu, 2017; Gu et al., 2020; Rempfer et al., 2017; Missiaen et al., 2020a). These studies generally forced the simulated AMOC into its off-state, allowing only for a limited comparability to our 9 Sv AMOC circulation state. Nevertheless, these studies found similar results to the ones described here, exhibiting an anti-correlation in the deep Atlantic from  $\sim 30^\circ\text{S}$ - $40^\circ\text{N}$  and a positive correlation in the  $\sim 0$ - $40^\circ\text{N}$  Atlantic. In the northern North Atlantic, the results by Missiaen et al. (2020a) resemble the fixed-particles response, whereas previous results from the Bern3D model by Rempfer et al. (2017); Süfke et al. (2020) are similar to the dynamic-particles case. However, the findings by Gu and Liu (2017) are remarkably different from our sensitivities and show little difference in the northern North Atlantic between their fixed-particles and their dynamic-particles cases. This is because Gu and Liu (2017) consider an AMOC shutdown state, which results in a very different particle response, with opal actually increasing in the northern North Atlantic and regionally different responses of POC and  $\text{CaCO}_3$ . In the Bern3D model, a complete AMOC collapse also induces an increase of opal in the northern North Atlantic (not shown). Thus, the particle responses

to an AMOC shutdown and an AMOC weakening are not directly comparable. Gu and Liu (2017) also investigated the time dependence of the Pa/Th response to a circulation change with accompanying dynamic particle response. They found that particle changes affect Pa/Th fastest, followed by the impact of AMOC change later in time. After equilibrium was established, the AMOC signal dominated over the particle signal in most regions, except at (40°N, 40°W, 4375 m) where they found a slight positive correlation between AMOC and Pa/Th as a result of the particle response. This qualitatively agrees with our results, as we only analysed equilibrium states and since their location of slight positive correlation lies close to where we found positive correlations (in region 1 (northern North Atlantic) north of 45°N; see upper right panel of Fig. 11).

Based on our model experiments, it emerges that the relationship between AMOC strength and Pa/Th is non-linear because AMOC changes are also directly linked to corresponding changes in particle concentrations also affecting Pa/Th. When the AMOC weakens, detecting the reduced NADW advection in Pa/Th becomes more challenging, although the induced particle response partly compensates for this. On the other hand, when the AMOC strengthens, the signal from NADW advection is large but the particle response with enhanced export production partly counteracts this.

### 3.4 Last Glacial Maximum

Finally, we investigate the last glacial maximum (LGM) sedimentary Pa/Th. Figure 12 shows measurements of Holocene and LGM sedimentary Pa/Th. The CTRL simulation is shown as a reference line. We do not show the weak AMOC runs here since they do not realistically represent LGM conditions as only the AMOC was adjusted. As in Fig. 10, we averaged over each region, because a single water column in the model is not sufficiently reliable. Simulated Pa/Th values of the CTRL are lower than Holocene sedimentary Pa/Th in region 1 (the northern North Atlantic) and 2 (the Bermuda Rise region). This offset is because sediment measurements reflect strong bottom scavenging (if any is present) simply because they are at the bottom, whereas modelled  $\text{Pa}_p/\text{Th}_p$  in the middle of a water column experiences less or no bottom scavenging. It would be fairer to only compare the bottom grid cells of the model (Fig. C5), but then model information from the overlying water column is not used, and this is very sensitive to the implementation of local bottom scavenging: Fig. C5 also shows that our bottom scavenging is too strong in the Bern3D model in regions 2, 4 and part of region 3. This can be due to our tuning of  $\sigma_{ne}^j$  to seawater data, where  $\sigma_{ne}^{\text{Pa}}$  was not well-constrained.

Now that we explained the offset in Pa/Th profiles between the simulated CTRL and Holocene measurements, we address the Holocene-LGM differences in Fig. 12. In region 2 (the Bermuda Rise), reconstructed Pa/Th are lower for the Holocene than LGM below 2.5 km. This indicates an anti-correlation between AMOC and Pa/Th in the sediments here, as is also simulated by the Bern3D model (Fig. 10b). The same behaviour is apparent in region 3 (the equatorial West Atlantic) below 2 km, where Holocene measurements agree very well with the CTRL. In region 1 (the northern North Atlantic) and

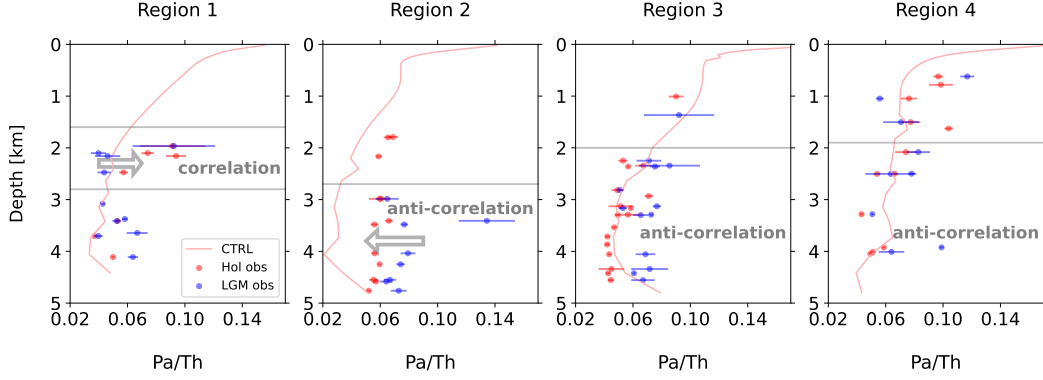


**Figure 12.** Sediment  $\text{Pa}_p/\text{Th}_p$  measurements (circles with error bars) in four regions of the West Atlantic (as in Fig. 3b) with the model CTRL  $\text{Pa}_p/\text{Th}_p$  repeated from Fig. 10b (17.8 Sv; represents the pre-industrial/Holocene). The other runs are not shown here because they do not resemble a realistic enough LGM state. Sediment cores from Fig. 3a/Table 2 that lie in the considered region are used. Arrows point in the direction of the supposed AMOC increase (from LGM to Holocene). Annotated text and grey lines indicate domains with an anti-correlation between  $\text{Pa}/\text{Th}$  and AMOC (arrow to left; Holocene left of LGM) respectively a correlation (arrow to right; Holocene right of LGM).

4 (the Southwest Atlantic), the qualitative relationship between  $\text{Pa}/\text{Th}$  and AMOC (i.e., anti-correlation or correlation) does not always agree between the model and reconstructions. Region 1 (the northern North Atlantic) has a correlation in both model and sediment at 2-3 km; below 3 km the model keeps this correlation signal, but reconstructions may show an anti-correlation in the scarce data here. This probably has to do with deep water formation located too far south in the Bern3D model, whereas in reality region 1 (the northern North Atlantic) only experiences NADW advection. In region 4 (the Southwest Atlantic), sediment data show an anti-correlation between AMOC and  $\text{Pa}/\text{Th}$ , just like region 2 and 3, but in the model we see no significant effect of AMOC weakening on  $\text{Pa}/\text{Th}$  here (Fig. 10b), probably because of cancelling imports and exports in the model here. Perhaps changes in dust at LGM – not captured in our simplified model experiments – were also important in this region. It is worth noting that modelled  $\text{Pa}/\text{Th}$  in region 4 exhibits a large spatial heterogeneity (Fig. C5), potentially corresponding to the ambiguous signal in sediment measurements here.

## 4 Conclusions and outlook

We improved the  $\text{Pa}/\text{Th}$  module of the Bern3D model by adding dust and spatially varying nepheloid layers (bottom scavenging) and we extensively retuned the particle sinking speed  $w_s$ , the 2 desorption constants  $k_{des}^j$ , and 10 scavenging parameters  $\sigma_i^j$ . The resulting CTRL simulation agrees well with present-day seawater observations and Holocene sediment core tops in the Atlantic, except in the Southern Ocean sector. Model experiments with different AMOC strengths and particle distributions demonstrate that North

Atlantic Pa/Th can still detect the NADW advection of a 9 Sv weak AMOC state in our estimates due to the AMOC-induced particle response at 40-60°N. A weaker AMOC transports fewer nutrients to the surface here (reduced lateral transport and reduced mixing with deep waters), which leads to fewer particles and more  $\text{Pa}_d$  available for advection in this source region. In the idealised case with no particle response the lowest limit of Pa/Th for recording a significant AMOC signal is at 11 Sv. Thus, the Pa-Th-AMOC system has a notable property: Pa/Th is more sensitive to AMOC change signals because of the way how biological particles respond to a weaker AMOC.

The sensitivity of Pa/Th to AMOC in different regions and depths of the Atlantic was explored in the model, as well as in published and new sediment core data from the Holocene and LGM. In both model and observations, AMOC strength is anti-correlated with Pa/Th in the deep equatorial West Atlantic and Bermuda Rise. The Bermuda Rise Pa/Th records are commonly considered as a reference indicator for AMOC, but both regions deserve attention, especially since the equatorial West Atlantic does not suffer from strong bottom scavenging and the resulting uncertainties in past bottom scavenging strength. Our findings suggest that Bermuda Rise Pa/Th contains a direct AMOC signal. In the South Atlantic, the model and sediment values do not agree, as the model seems to be insensitive to AMOC changes, while a clear signal is found in the reconstructions. Lastly, the northern North Atlantic (region 1) possesses a positive correlation between Pa/Th and AMOC in the model as well as in 0-3 km sediment. In the model, the reason for this positive correlation is the strong AMOC-induced particle response here – this is the only difference between the simulations in Fig. 10a and b. Cores in this region with high opal from the northern opal belt are actually promising for the reconstruction of AMOC variations when we embrace their positive correlation between Pa/Th and AMOC in (part of) the 40-60°N Atlantic.

In this study we contributed to an improved understanding of the AMOC proxy in the Atlantic, but we were not yet able to make a quantitative estimate of the LGM AMOC. Despite certain knowledge gaps, the Pa/Th proxy presents a high potential to reliably quantify past AMOC changes. To overcome these knowledge gaps, more Pa/Th modelling studies are needed, focused on the same goals (see below). Further, additional sediment cores in the 40-60°N North Atlantic between 1 and 2 km of the water column depth are desirable, especially close to locations of known positive correlation (such as cores 12, 15, and 20). A reinterpretation of down-core records recovered from regions 1, 2 and 3 should be performed based on the new insights gained in this study and future modelling studies.

Possibilities for follow-up studies with the Bern3D model are: (i) find a better way to tune  $\sigma_{ne}^j$ , the coefficients of scavenging to nepheloid-layer particles (Table 3); (ii) investigate a collapsed AMOC state, which exhibits a very different circulation; and (iii) make particle remineralisation curves, which are currently globally uniform in the Bern3D model (Eq. (2)-(4)), depend on local characteristics such as temperature by coupling to the new particle model MSPACMAM (Dinauer et al., 2022).



Modelling studies use widely different scavenging parameters, either found by tuning or chosen from the wide range of observational literature (Supplementary Dataset S3). It would be important to better constrain the ranges of scavenging parameters, which would also improve the comparability between studies. Here the absolute values are not of much importance, but the ratios between the parameters are. Computationally more expensive models could still perform many steady state tuning runs by using Anderson Acceleration (Khatiwala, 2023). An alternative to tuning is taking over the scavenging parameter set from another modelling study if this directly yields satisfying Pa-Th results in the model at hand (not only for the Pa/Th ratio but also for the separate forms). Scavenging coefficients and partition coefficients can be converted into each other as shown in Supplementary Dataset S3.

More modelling studies of weakened AMOC states are also desirable to confirm the large potential we saw in the equatorial West Atlantic, and to assess the particle response to an AMOC weakening in the Bern3D model. A hypothesis for the model-sediment mismatch in the northern North Atlantic Pa/Th profile is a possibly too strong particle response in the Bern3D model here. Another possible reason is a too far south deep water formation in the Bern3D. If another model would perform better in region 1 (i.e., fit well with Holocene sediment), then this model could be used to quantify how much AMOC decrease a certain decrease in northern north Atlantic Pa/Th corresponds to. In fact, if the same model also fits well with Holocene sediment in regions 2 and 3, like the Bern3D (see Fig. 12 and C5), the Pa/Th response to AMOC can be quantified there as well.

In conclusion, we have presented a detailed modelling study, combined with new Pa/Th data, and provided a new regional-scale analysis of detectability of, and sensitivity to, AMOC changes by this paleoceanographic tracer. Combining it with other, complementary tracers will further enhance its usefulness in reconstructing past ocean circulation changes and their regional signals.



## Appendix A The diagnostic and prognostic approach of modelling Pa and Th

In this section, we clarify the two most common approaches of implementing Pa and Th used in three-dimensional models with a dynamically simulated ocean, but which are rarely explained. We name the two main approaches the diagnostic and the prognostic approach, according to their governing equations (see below). Diagnostic refers to the approach of determining (diagnosing) dissolved and particulate tracer concentration from a simulated total concentration.

The governing equations of the diagnostic approach are (Gu & Liu, 2017):

$$\frac{\partial A_{\text{total}}^j}{\partial t} = \text{Transport} \left( A_{\text{total}}^j \right) - \lambda^j A_{\text{total}}^j + \beta^j - w_s \frac{\partial A_p^j}{\partial z}, \quad (\text{A1})$$

$$A_d^j = \frac{1}{1 + \frac{1}{\rho_{sw}} \left( K_{\text{POC}}^j C_{\text{POC}} + K_{\text{ca}}^j C_{\text{ca}} + K_{\text{op}}^j C_{\text{op}} + K_{\text{du}}^j C_{\text{du}} \right)} \cdot A_{\text{total}}^j, \quad (\text{A2})$$

$$A_p^j = \left( 1 - \frac{1}{1 + \frac{1}{\rho_{sw}} \left( K_{\text{POC}}^j C_{\text{POC}} + K_{\text{ca}}^j C_{\text{ca}} + K_{\text{op}}^j C_{\text{op}} + K_{\text{du}}^j C_{\text{du}} \right)} \right) \cdot A_{\text{total}}^j, \quad (\text{A3})$$

whereas the prognostic approach is formulated as (Rempfer et al., 2017):

$$\frac{\partial A_d^j}{\partial t} = \text{Transport} \left( A_d^j \right) - \lambda^j A_d^j + k_{\text{des}}^j A_p^j - k_{\text{ads}}^j A_d^j + \beta^j, \quad (\text{A4})$$

$$\frac{\partial A_p^j}{\partial t} = \text{Transport} \left( A_p^j \right) - \lambda^j A_p^j - k_{\text{des}}^j A_p^j + k_{\text{ads}}^j A_d^j - w_s \frac{\partial A_p^j}{\partial z}. \quad (\text{A5})$$

It is evident that the prognostic approach is physically more realistic as it simulates the different processes individually. The advantage of the diagnostic approach on the other hand is that it is computationally lighter.

Variables and parameters are listed in Table 1 of the main text. The tracers are subject to oceanic transport (advection, convection and diffusion). Sources and sinks are radioactive decay  $\lambda^j$ , radioactive production  $\beta^j$  and scavenging by sinking particles with sinking speed  $w_s$ . The approaches simulate reversible scavenging by sinking particles differently. The diagnostic approach uses particle mass concentrations  $C_i$ , seawater density  $\rho_{sw}$  and fixed partition coefficients, or distribution coefficients,  $(K_d)_i^j = K_i^j$ , which govern the ratio of particle-bound to dissolved concentration (Gu & Liu, 2017):

$$K_i^j = \frac{\rho_{sw}}{C_i} \frac{A_{p,i}^j}{A_d^j} \quad (\text{A6})$$

$$i \in [\text{POC}, \text{CaCO}_3, \text{opal}, \text{dust}, \text{neph}]$$

$$j \in [\text{Pa}, \text{Th}]$$

with  $A_{p,i}^j$  the part of  $A_p^j$  that is bound to particle type  $i$ . Particle types  $i$  vary between studies, especially whether dust and nepheloid-layer particles are present. The prognostic approach instead simulates scavenging via adsorption and desorption coefficients:

$$k_{\text{ads}}^j(\theta, \phi, z) = \sum_i \sigma_i^j \cdot F_i(\theta, \phi, z), \quad (\text{A7})$$

$$k_{\text{des}}^j = 2.4 \text{ yr}^{-1}, \quad (\text{A8})$$

$$i \in [POC, CaCO_3, opal, dust, neph]$$

$$j \in [Pa, Th]$$

where  $\sigma_i^j$  are globally fixed scavenging coefficients expressing how strongly particle type  $i$  adsorbs tracer  $j$ , and where  $F_i(\theta, \phi, z)$  is the downward flux of particle  $i$  in grid cell  $(\theta, \phi, z)$ . The scavenging parameters of the two approaches (partition coefficients  $K_i^j$  respectively scavenging coefficients  $\sigma_i^j$ ) can be converted into one another via Missiaen et al. (2020a):

$$K_i^j = \frac{w_s \cdot \rho_{sw} \cdot \sigma_i^j}{M_i \cdot k_{\text{des}}^j}, \quad (\text{A9})$$

where  $M_i$  is the molar mass. This relationship allows us to compare results between all studies. We used the  $M_i$  with units based on Bern3D model units:  $M_{POC} = M_{ca} = 12 \text{ g/mol}$  (simulated in mol C),  $M_{op} = 28 \text{ g/mol}$  (simulated in mol Si) and  $M_{du} = M_{ne} = 1$  the conversion factors for dust and nepheloid-layer particles (already simulated in g).

The diagnostic approach was introduced by Henderson et al. (1999) in the HAMOCC model and is used in the Bern3D model (Siddall et al., 2005), the NEMO model (Dutay et al., 2009; van Hulten et al., 2018), the CESM (Gu & Liu, 2017) and the COCO model (Sasaki et al., 2022). The prognostic approach was introduced by Marchal et al. (2000) and is applied in the Bern3D model (Rempfer et al., 2017), the POM (Princeton Ocean Model; Lerner et al. (2020)) and the iLOVECLIM model (Missiaen et al., 2020a). The approaches are not equivalent, but both have their advantages and disadvantages. The diagnostic approach has the advantage that (1) the computational cost is reduced; and (2) the usage of  $K_i^j$  is analogous to common implementations of other paleoceanographic tracers such as neodymium (Arsouze et al., 2009; Rempfer et al., 2011; Gu et al., 2019) and beryllium (Heinze et al., 2006; Li et al., 2021). On the other hand, the prognostic approach (1) allows for disequilibrium between adsorption and desorption. Although desorption-adsorption equilibrium already establishes on the order of several months (Bacon & Anderson, 1982), this can make a difference in regions where seasonal effects are important, for instance during deep water formation.

## Appendix B Corrections to equation in Rempfer et al. (2017)

The tuning results from this study were compared to Rempfer et al. (2017) in Table 3 of the main text, where we corrected their result for typos in their equation, as explained here. Rempfer et al. (2017) define the fractionation factor as  $f_i = f_i(Th/Pa) = K_i^{Th}/K_i^{Pa}$  and  $g_{ca,op}^{Pa} := \sigma_{ca}^{Pa}/\sigma_{op}^{Pa}$  and then they give their scavenging coefficients  $\sigma_i^j$  in their equation (5a)-(6b), which we repeat here:

$$\sigma_{POC}^{Pa} = \sigma_0 \cdot f_{POC} \quad (B1)$$

$$\sigma_{ca}^{Pa} = \sigma_0 \cdot f_{ca} \quad (B2)$$

$$\sigma_{op}^{Pa} = \sigma_0 \cdot f_{ca} \cdot g_{ca,op}^{Pa} = \sigma_{ca}^{Pa} \cdot g_{ca,op}^{Pa} \quad (B3)$$

$$\sigma_{litho}^{Pa} = \sigma_0 \cdot f_{litho} \quad (B4)$$

$$\sigma_{POC,ca,litho}^{Th} = \sigma_0 \cdot 1 \quad (B5)$$

$$\sigma_{op}^{Th} = \sigma_0 \cdot f_{ca} \cdot g_{ca,op}^{Pa} \cdot f_{op}^{-1} = \sigma_{op}^{Pa} \cdot f_{op}^{-1}, \quad (B6)$$

where they use  $\sigma_0 = 1$ ,  $f_{POC} = 1$ ,  $f_{op} = 1$  and  $f_{ca} = 10$ ,  $f_{litho} = 10$ ,  $g_{ca,op}^{Pa} = 1$  (given in their Table A2). Our proposed correct formulation of their Equation (5a)-(6b) is:

$$\sigma_{POC}^{Pa} = \sigma_0 \cdot f_{POC}^{-1} \quad (B7)$$

$$\sigma_{ca}^{Pa} = \sigma_0 \cdot f_{ca}^{-1} \quad (B8)$$

$$\sigma_{op}^{Pa} = \sigma_0 \cdot f_{ca}^{-1} \cdot (g_{ca,op}^{Pa})^{-1} = \sigma_{ca}^{Pa} \cdot (g_{ca,op}^{Pa})^{-1} \quad (B9)$$

$$\sigma_{litho}^{Pa} = \sigma_0 \cdot f_{litho}^{-1} \quad (B10)$$

$$\sigma_{POC,ca,litho}^{Th} = \sigma_0 \cdot 1 \quad (B11)$$

$$\sigma_{op}^{Th} = \sigma_0 \cdot f_{ca}^{-1} \cdot (g_{ca,op}^{Pa})^{-1} \cdot f_{op} = \sigma_{op}^{Pa} \cdot f_{op}, \quad (B12)$$

because in order to go from Th (which has  $\sigma_i^{Th} = \sigma_0$  for most  $i$ ) to Pa one needs to divide by  $f_i$  – as is also done in Marchal et al. (2000); analogously for  $g_{ca,op}^{Pa}$ . The latter formulation gives the  $\sigma_i^j$  as in Table 3, whereas the original equations give  $\sigma_{ca}^{Pa} = 10 \cdot \sigma_{ca}^{Th}$ , which contradicts the idea of the protactinium-thorium proxy. Inspection of the code of the Bern3D model version 1.0 demonstrated that these typos had no impact on the results presented in Rempfer et al. (2017), since the  $\sigma_i^j$  values are read in as parameters directly instead of via the equations above.

In addition, the caption of their figure 2 mentions “along GEOTRACES transect GA03 (Hayes et al., 2015a)”. Based on the map in their figure A4, this should rather be: “along GEOTRACES transect GA03 (Hayes et al., 2015a) until the crossing with GA02, and then continuing northwards on GA02”.

## Appendix C Additional figures and tables

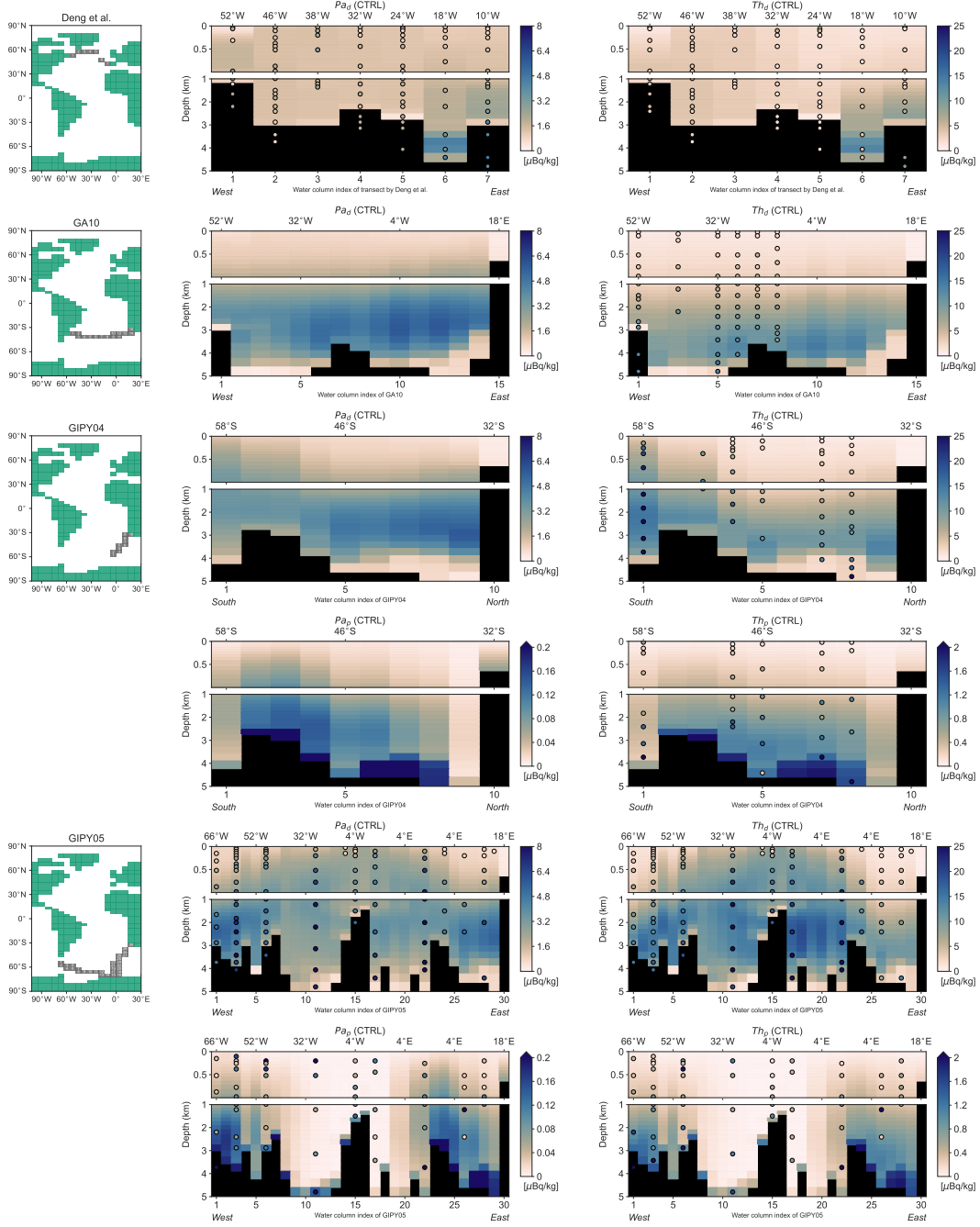


**Figure C1.** CTRL model output (background) with seawater observations (circles) along more transects in the Atlantic and the Atlantic sector of the Southern Ocean for  $Pa_d$ ,  $Th_d$ ,  $Pa_p$  and  $Th_p$  (where available). Data references in Sect. 2.3. Numbering on the transect maps (left) defines the order of plotting and corresponds to the water column indices on the  $x$ -axis of that transect. Seawater data circles are plotted centred in the nearest model grid cell box. If a grid cell contains multiple seawater observations, an uncertainty-weighted average is taken.

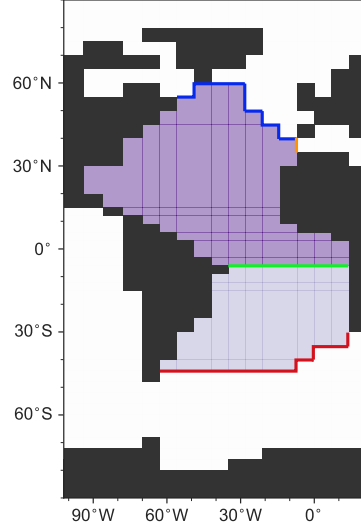


**Figure C2.** Definition of North Atlantic and South Atlantic sub-basins as used for budget calculations: confined by GEOVIDE (blue), WOCE A07 (green) and WOCE A11 (red), transferred to the Bern3D model grid. The boundary with the Mediterranean Sea (MED; orange) is also used in the budget calculation.

**Table C1.** Additional model runs used in Fig. 8, in addition to runs in Table 4 of the main text. All simulations were run into steady state for 5,000 years. All runs have the same parameter settings, dust and nepheloid particles as CTRL, unless indicated otherwise. Biological particles comprise POC,  $\text{CaCO}_3$  and opal.

Runname	AMOC	Forcing <sup>a</sup>	Biological particles <sup>b</sup>	Description
P/2_18Sv	17.8 Sv	-	$\times 0.5$	Half of CTRL particles
P/2_14Sv	13.9 Sv	0.10	$\times 0.5$	$\sim 14$ Sv AMOC; particles fixed to $0.5 \times \text{CTRL}$
P/2_11Sv	11.2 Sv	0.15	$\times 0.5$	$\sim 11$ Sv AMOC; particles fixed to $0.5 \times \text{CTRL}$
P/2_9Sv	8.6 Sv	0.20	$\times 0.5$	etc.
Px2_18Sv	17.8 Sv	-	$\times 2$	Double of CTRL particles
Px2_14Sv	13.9 Sv	0.10	$\times 2$	$\sim 14$ Sv AMOC; particles fixed to $2 \times \text{CTRL}$
Px2_11Sv	11.2 Sv	0.15	$\times 2$	etc.
Px2_9Sv	8.6 Sv	0.20	$\times 2$	
Px3_18Sv	17.8 Sv	-	$\times 3$	Triple of CTRL particles
Px3_14Sv	13.9 Sv	0.10	$\times 3$	
Px3_11Sv	11.2 Sv	0.15	$\times 3$	
Px3_9Sv	8.6 Sv	0.20	$\times 3$	
Px5_18Sv	17.8 Sv	-	$\times 5$	CTRL particles times 5
Px5_14Sv	13.9 Sv	0.10	$\times 5$	
Px5_11Sv	11.2 Sv	0.15	$\times 5$	
Px5_9Sv	8.6 Sv	0.20	$\times 5$	

<sup>a</sup>Freshwater forcing [Sv] in the North Atlantic between  $45^\circ\text{N}$  and  $70^\circ\text{N}$ .

<sup>b</sup>All runs here have biological particles fixed to (yearly avg.) particles from CTRL  $\times$  a factor.

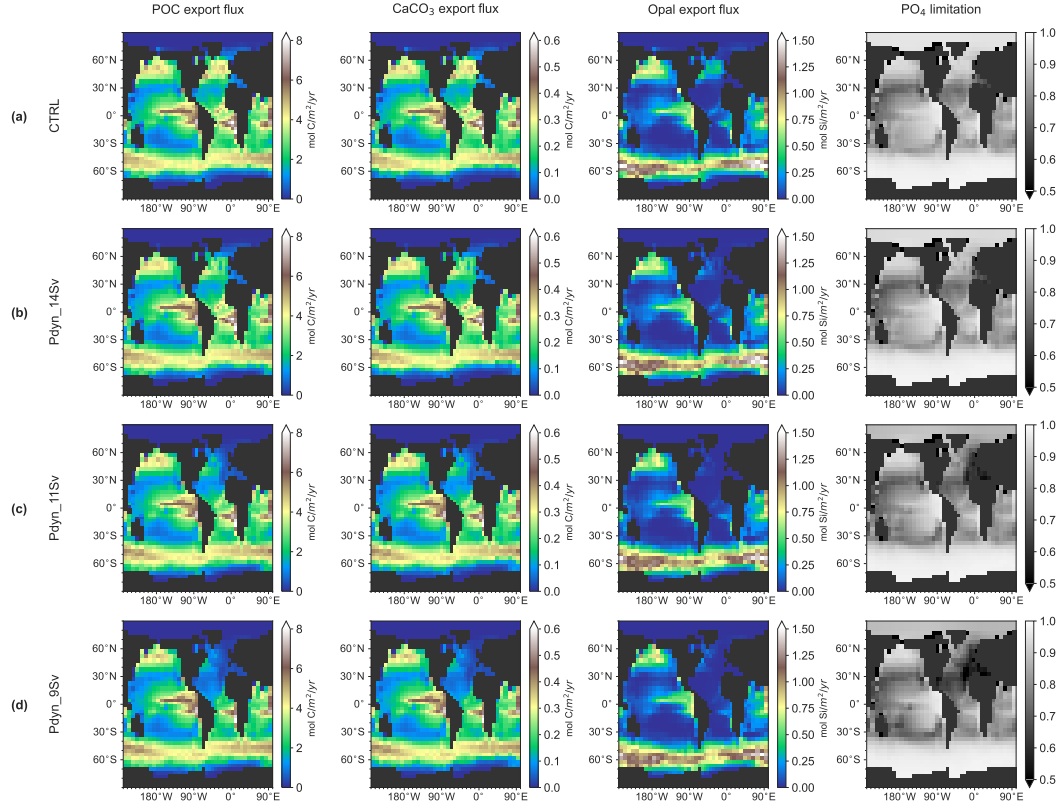


**Figure C3.** Export production of particulate organic carbon (POC), calcium carbonate and opal, induced by different ocean circulation states corresponding to AMOC strengths of (a) the CTRL run (CTRL = Pdyn\_18Sv; equal to Fig. 2a-c) and for runs with a weakened AMOC of (b) 14 Sv, (c) 11 Sv and (d) 9 Sv. Also plotted is the limiting factor of surface PO<sub>4</sub> concentrations on particle growth (right-most column; 1 is no limitation, 0 is total limitation). Patterns of POC and CaCO<sub>3</sub> are identical, because CaCO<sub>3</sub> entirely depends on POC in the Bern3D model (not entirely realistic).

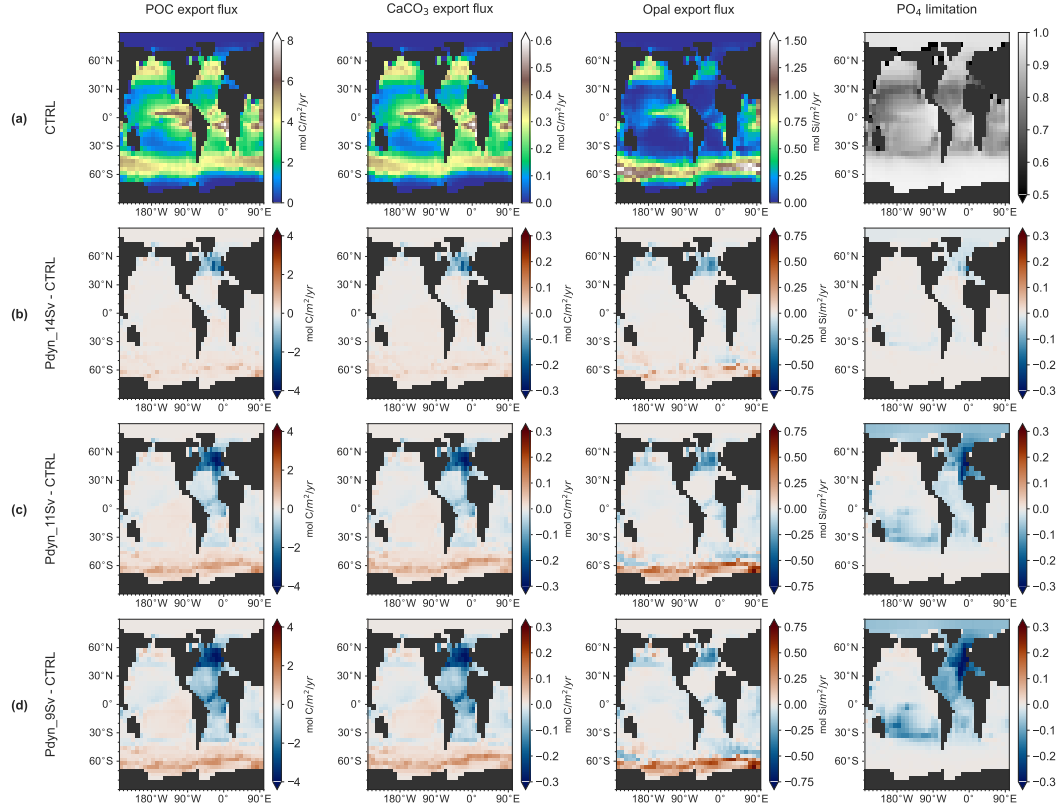


**Figure C4.** Export production: as Fig. C3, but now the anomalies with respect to row (a) are shown.

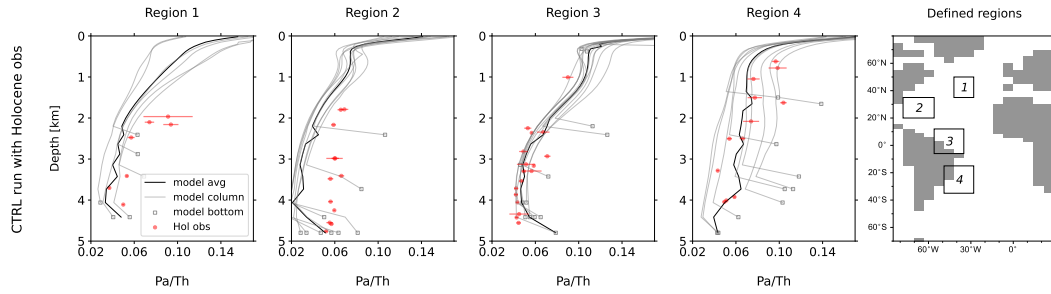


**Figure C5.** Modelled  $\text{Pa}_p/\text{Th}_p$  of the CTRL (lines) and sediment  $\text{Pa}_p/\text{Th}_p$  measurements (red circles with error bars) for the Holocene (0-8 ka) in four regions of the West Atlantic. This represents present-day conditions. The black line is the average of the grey lines, which are the 6, 9, 14 and 10 model water columns of the region under consideration. Bottom cells are emphasised with grey open squares. The fairest comparison is obtained when only comparing model bottom values (grey open squares) to sediment observations (red closed circles).

## Open Research

New sediment measurements of this study are available at PANGAEA (XXXX) and in Supplementary Dataset S2. Supplementary Dataset S2 also provides the age models. The Bern3D model is closed-source, but the output of model simulations used in this study is available in netCDF format on zenodo (Scheen et al., 2024a). The output of the many tuning runs is not available, yet their  $(w_s, k_{des}^j, \sigma_i^j)$  parameter settings and resulting MAEs can be found in the csv files of the same repository (Scheen et al., 2024a). The code to analyse the model runs and to generate the figures is shared in another repository (Scheen et al., 2024b) in well-documented python notebooks. Finally, Supplementary Dataset S3 contains the literature compilation of scavenging parameters (used to determine the tuning range). In the case of questions or suspected bugs, please contact the corresponding author Jeemijn Scheen.

## Acknowledgments

This research was supported by the Swiss National Science Foundation (grants no. SNF 200020\_172745 and 200020\_200492, awarded to TFS) and the Deutsche Forschungsgemeinschaft (grant no. LI1815/4, awarded to JL). FP was financially supported by the European Union’s Horizon 2020 research and innovation program (grant no. 101023443; project CliMoTran). We gratefully acknowledge Christoph C. Raible for helpful comments on an earlier version of the manuscript. We thank Janne Repschläger, Delia Oppo, Lars Max, Samuel Jaccard and the ODP core repository in Bremen for providing sediment sample material. We thank Marcel Regelous for enabling the ICP-MS measurements at the GeoCenter Northern Bavaria, Erlangen. We thank Feifei Deng and Lise Misaen for answering questions about their papers. We thank Alexey Mishonov, Mary Jo Richardson and Wilford Gardner for providing the data behind their figures (later published as Gardner et al. (2020)). Calculations were performed on UBELIX, the high-performance computing cluster at the University of Bern. We used python with a.o. the package cmcramer for colour maps (Cramer, 2023), xESMF for regridding (Zhuang et al., 2023) and plotting routines from Scheen (2020). We made use of the GEOTRACES 2021 Intermediate Data Product (IDP2021), which represents an international collaboration and is endorsed by the Scientific Committee on Oceanic Research (SCOR). The many researchers and funding agencies responsible for the collection of data and quality control are thanked for their contributions to the IDP2021.

Author contributions: JS carried out the numerical simulations, model development including tuning and the analysis. JL compiled the sediment measurements from literature and had a leading role in the design of the research questions. FP helped with model development and interpretation. FS performed the sediment measurements together with JL. TFS conceived the original idea and supervised the project. JS led the writing of the paper with JL, FP and TFS contributing substantially to the text and the interpretation of the results.



## References

- Abrantes, F. (2000). 200000 yr diatom records from Atlantic upwelling sites reveal maximum productivity during LGM and a shift in phytoplankton community structure at 185000 yr. *Earth and Planetary Science Letters*, 176, 7–16. doi: 10.1016/S0012-821X(99)00312-X
- Anderson, R. F., Bacon, M. P., & Brewer, P. G. (1983). Removal of  $^{230}\text{Th}$  and  $^{231}\text{Pa}$  from the open ocean. *Earth and Planetary Science Letters*, 62, 7–23. doi: 10.1016/0012-821X(83)90067-5
- Anderson, R. F., Barker, S., Fleisher, M., Gersonde, R., Goldstein, S. L., Kuhn, G., Mortyn, P. G., Pahnke, K., & Sachs, J. P. (2014). Biological response to millennial variability of dust and nutrient supply in the Subantarctic South Atlantic Ocean. *Philosophical Transactions of the Royal Society A: Mathematical, Physical and Engineering Sciences*, 372, 20130054. doi: 10.1098/rsta.2013.0054
- Anderson, R. F., Cheng, H., Edwards, R. L., Fleisher, M. Q., Hayes, C. T., Huang, K.-F., Kadko, D., Lam, P. J., Landing, W. M., Lao, Y., Lu, Y., Measures, C. I., Moran, S. B., Morton, P. L., Ohnemus, D. C., Robinson, L. F., & Shelly, R. U. (2016). How well can we quantify dust deposition to the ocean? *Philosophical Transactions of the Royal Society A: Mathematical, Physical and Engineering Sciences*, 374, 20150285. doi: 10.1098/rsta.2015.0285
- Arsouze, T., Dutay, J.-C., Lacan, F., & Jeandel, C. (2009). Reconstructing the Nd oceanic cycle using a coupled dynamical–biogeochemical model. *Biogeosciences*, 6, 2829–2846. doi: 10.5194/bg-6-2829-2009
- Bacon, M. P., & Anderson, R. F. (1982). Distribution of thorium isotopes between dissolved and particulate forms in the deep sea. *Journal of Geophysical Research: Oceans*, 87, 2045–2056. doi: 10.1029/JC087iC03p02045
- Blaauw, M., & Christen, J. A. (2011). Flexible paleoclimate age-depth models using an autoregressive gamma process. *Bayesian Analysis*, 6, 457–474. doi: 10.1214/11-BA618
- Böhm, E., Lippold, J., Gutjahr, M., Frank, M., Blaser, P., Antz, B., Fohlmeister, J., Frank, N., Andersen, M. B., & Deininger, M. (2015). Strong and deep Atlantic meridional overturning circulation during the last glacial cycle. *Nature*, 517, 73–76. doi: 10.1038/nature14059
- Bourne, M. D., Thomas, A. L., Mac Niocaill, C., & Henderson, G. M. (2012). Improved determination of marine sedimentation rates using  $^{230}\text{Th}_{\text{xs}}$ . *Geochemistry, Geophysics, Geosystems*, 13, 1–9. doi: 10.1029/2012GC004295
- Bradt Miller, L. I., Anderson, R. F., Fleisher, M. Q., & Burckle, L. H. (2007). Opal burial in the equatorial Atlantic Ocean over the last 30 ka: Implications for glacial-interglacial changes in the ocean silicon cycle. *Paleoceanography*, 22(4). doi: 10.1029/2007PA001443
- Bradt Miller, L. I., McManus, J. F., & Robinson, L. F. (2014).  $^{231}\text{Pa}/^{230}\text{Th}$  evidence for a weakened but persistent Atlantic meridional overturning cir-

- ulation during Heinrich Stadial 1. *Nature Communications*, 5(1). doi: 10.1038/ncomms6817
- Burckel, P., Waelbroeck, C., Gherardi, J. M., Pichat, S., Arz, H., Lippold, J., Dokken, T., & Thil, F. (2015). Atlantic Ocean circulation changes preceded millennial tropical South America rainfall events during the last glacial. *Geophysical Research Letters*, 42, 411–418. doi: 10.1002/2014GL062512
- Burckel, P., Waelbroeck, C., Luo, Y., Roche, D. M., Pichat, S., Jaccard, S. L., Gherardi, J., Govin, A., Lippold, J., & Thil, F. (2016). Changes in the geometry and strength of the Atlantic meridional overturning circulation during the last glacial (20–50 ka). *Climate of the Past*, 12, 2061–2075. doi: 10.5194/cp-12-2061-2016
- Burke, A., Marchal, O., Bradtmiller, L. I., McManus, J. F., & François, R. (2011). Application of an inverse method to interpret  $^{231}\text{Pa}/^{230}\text{Th}$  observations from marine sediments. *Paleoceanography*, 26(1). doi: 10.1029/2010PA002022
- Cael, B. B., Cavan, E. L., & Britten, G. L. (2021). Reconciling the size-dependence of marine particle sinking speed. *Geophysical Research Letters*, 48, e2020GL091771. doi: 10.1029/2020GL091771
- Carroll, D., & Starkey, H. C. (1958). Effect of sea-water on clay minerals. *Clays and Clay Minerals*, 7, 80–101. doi: 10.1346/CCMN.1958.0070103
- Chase, Z., & Anderson, R. F. (2004). Comment on “on the importance of opal, carbonate, and lithogenic clays in scavenging and fractionating  $^{230}\text{Th}$ ,  $^{231}\text{Pa}$  and  $^{10}\text{Be}$  in the ocean” by S. Luo and T.-L. Ku. *Earth and Planetary Science Letters*, 220, 213–222. doi: 10.1016/S0012-821X(04)00028-7
- Chase, Z., Anderson, R. F., Fleisher, M. Q., & Kubik, P. W. (2002). The influence of particle composition and particle flux on scavenging of Th, Pa and Be in the ocean. *Earth and Planetary Science Letters*, 204, 215–229. doi: 10.1016/S0012-821X(02)00984-6
- Chen, J. H., Lawrence Edwards, R., & Wasserburg, G. J. (1986).  $^{238}\text{U}$ ,  $^{234}\text{U}$  and  $^{232}\text{Th}$  in seawater. *Earth and Planetary Science Letters*, 80, 241–251. doi: 10.1016/0012-821X(86)90108-1
- Chen, S.-Y. S., Marchal, O., Lerner, P. E., McCorkle, D. C., & Rutgers van der Loeff, M. M. (2021). On the cycling of  $^{231}\text{Pa}$  and  $^{230}\text{Th}$  in benthic nepheloid layers. *Deep Sea Research Part I: Oceanographic Research Papers*, 177, 103627. doi: 10.1016/j.dsr.2021.103627
- Crameri, F. (2023). *Scientific colour maps* [Software]. Zenodo. doi: 10.5281/zenodo.8035877
- Deng, F., Henderson, G. M., Castrillejo, M., Perez, F. F., & Steinfeldt, R. (2018). Evolution of  $^{231}\text{Pa}$  and  $^{230}\text{Th}$  in overflow waters of the North Atlantic. *Biogeosciences*, 15, 7299–7313. doi: 10.5194/bg-15-7299-2018
- Deng, F., Thomas, A. L., Rijkenberg, M. J., & Henderson, G. M. (2014). Controls on seawater  $^{231}\text{Pa}$ ,  $^{230}\text{Th}$  and  $^{232}\text{Th}$  concentrations along the flow paths of deep waters in the Southwest Atlantic. *Earth and Planetary Science Letters*, 390, 93–102. doi: 10.1016/j.epsl.2013.12.038

- Dinauer, A., Laufkötter, C., Doney, S. C., & Joos, F. (2022). What controls the large-scale efficiency of carbon transfer through the ocean's mesopelagic zone? insights from a new, mechanistic model (MSPACMAM). *Global Biogeochemical Cycles*, *36*, e2021GB007131. doi: 10.1029/2021GB007131
- Dutay, J.-C., Lacan, F., Roy-Barman, M., & Bopp, L. (2009). Influence of particle size and type on  $^{231}\text{Pa}$  and  $^{230}\text{Th}$  simulation with a global coupled biogeochemical-ocean general circulation model: A first approach. *Geochemistry, Geophysics, Geosystems*, *10*(1). doi: 10.1029/2008GC002291
- Edwards, N. R., Willmott, A. J., & Killworth, P. D. (1998). On the role of topography and wind stress on the stability of the thermohaline circulation. *Journal of Physical Oceanography*, *28*, 756–778. doi: 10.1175/1520-0485(1998)028<0756:OTROTA>2.0.CO;2
- Fietzke, J., Bollhöfer, A., Frank, N., & Mangini, A. (1999). Protactinium determination in manganese crust VA13/2 by thermal ionization mass spectrometry (TIMS). *Nuclear Instruments and Methods in Physics Research Section B: Beam Interactions with Materials and Atoms*, *149*, 353–360. doi: 10.1016/S0168-583X(98)00912-4
- Gardner, W. D., Mishonov, A. V., & Richardson, M. J. (2020). *Global transmissometer database v3* [Dataset]. Retrieved from <https://odv.awi.de/data/ocean/global-transmissometer-database/>
- Gardner, W. D., Richardson, M. J., & Mishonov, A. V. (2018b). Global assessment of benthic nepheloid layers and linkage with upper ocean dynamics. *Earth and Planetary Science Letters*, *482*, 126–134. doi: 10.1016/j.epsl.2017.11.008
- Gardner, W. D., Richardson, M. J., Mishonov, A. V., & Biscaye, P. E. (2018a). Global comparison of benthic nepheloid layers based on 52 years of nephelometer and transmissometer measurements. *Progress in Oceanography*, *168*, 100–111. doi: 10.1016/j.pocean.2018.09.008
- Gebbie, G. (2014). How much did Glacial North Atlantic Water shoal? *Paleoceanography*, *29*, 190–209. doi: 10.1002/2013PA002557
- Geibert, W., & Usbeck, R. (2004). Adsorption of thorium and protactinium onto different particle types: experimental findings. *Geochimica et Cosmochimica Acta*, *68*, 1489–1501. doi: 10.1016/j.gca.2003.10.011
- GEOTRACES Intermediate Data Product Group. (2021). The GEOTRACES Intermediate Data Product 2021 (IDP2021). *NERC EDS British Oceanographic Data Centre NOC*. (last accessed 30-11-2021) doi: 10.5285/cf2d9ba9-d51d-3b7c-e053-8486abc0f5fd
- Gherardi, J.-M., Labeyrie, L., McManus, J., François, R., Skinner, L., & Cortijo, E. (2005). Evidence from the Northeastern Atlantic basin for variability in the rate of the meridional overturning circulation through the last deglaciation. *Earth and Planetary Science Letters*, *240*, 710–723. doi: 10.1016/j.epsl.2005.09.061
- Gherardi, J.-M., Labeyrie, L., Nave, S., François, R., McManus, J. F., & Cortijo, E. (2009). Glacial-interglacial circulation changes inferred from  $^{231}\text{Pa}/^{230}\text{Th}$

- sedimentary record in the North Atlantic region. *Paleoceanography*, *24*(2). doi: 10.1029/2008PA001696
- Gottschalk, J., Szidat, S., Michel, E., Mazaud, A., Salazar, G., Battaglia, M., Lipold, J., & Jaccard, S. L. (2018). Radiocarbon measurements of small-size foraminiferal samples with the Mini Carbon Dating System (MICADAS) at the University of Bern: Implications for paleoclimate reconstructions. *Radiocarbon*, *60*, 469–491. doi: 10.1017/RDC.2018.3
- Gu, S., & Liu, Z. (2017).  $^{231}\text{Pa}$  and  $^{230}\text{Th}$  in the ocean model of the Community Earth System Model (CESM1.3). *Geoscientific Model Development*, *10*, 4723–4742. doi: 10.5194/gmd-10-4723-2017
- Gu, S., Liu, Z., Jahn, A., Rempfer, J., Zhang, J., & Joos, F. (2019). Modeling neodymium isotopes in the ocean component of the Community Earth System Model (CESM1). *Journal of Advances in Modeling Earth Systems*, *11*, 624–640. doi: 10.1029/2018MS001538
- Gu, S., Liu, Z., Oppo, D. W., Lynch-Stieglitz, J., Jahn, A., Zhang, J., & Wu, L. (2020). Assessing the potential capability of reconstructing glacial Atlantic water masses and AMOC using multiple proxies in CESM. *Earth and Planetary Science Letters*, *541*, 116294. doi: 10.1016/j.epsl.2020.116294
- Hall, I. R., Moran, S. B., Zahn, R., Knutz, P. C., Shen, C.-C., & Edwards, R. L. (2006). Accelerated drawdown of meridional overturning in the late-glacial Atlantic triggered by transient pre-H event freshwater perturbation. *Geophysical Research Letters*, *33*(16). doi: 10.1029/2006GL026239
- Hayes, C. T., Anderson, R. F., Fleisher, M. Q., Huang, K.-F., Robinson, L. F., Lu, Y., Cheng, H., Edwards, R. L., & Moran, S. B. (2015b).  $^{230}\text{Th}$  and  $^{231}\text{Pa}$  on GEOTRACES GA03, the U.S. GEOTRACES North Atlantic transect, and implications for modern and paleoceanographic chemical fluxes. *Deep Sea Research Part II: Topical Studies in Oceanography*, *116*, 29–41. doi: 10.1016/j.dsr2.2014.07.007
- Hayes, C. T., Anderson, R. F., Fleisher, M. Q., Vivancos, S. M., Lam, P. J., Ohnenmus, D. C., Huang, K.-F., Robinson, L. F., Lu, Y., Cheng, H., Edwards, R. L., & Moran, S. B. (2015a). Intensity of Th and Pa scavenging partitioned by particle chemistry in the North Atlantic Ocean. *Marine Chemistry*, *170*, 49–60. doi: 10.1016/j.marchem.2015.01.006
- Hayes, C. T., Anderson, R. F., Jaccard, S. L., François, R., Fleisher, M. Q., Soon, M., & Gersonde, R. (2013). A new perspective on boundary scavenging in the North Pacific Ocean. *Earth and Planetary Science Letters*, *369–370*, 86–97. doi: 10.1016/j.epsl.2013.03.008
- Hayes, C. T., Rosen, J., McGee, D., & Boyle, E. A. (2017). Thorium distributions in high- and low-dust regions and the significance for iron supply. *Global Biogeochemical Cycles*, *31*, 328–347. doi: 10.1002/2016GB005511
- Heaton, T. J., Köhler, P., Butzin, M., Bard, E., Reimer, R. W., Austin, W. E. N., Bronk Ramsey, C., Grootes, P. M., Hughen, K. A., Kromer, B., Reimer, P. J., Adkins, J., Burke, A., Cook, M. S., Olsen, J., & Skinner, L. C. (2020). Ma-

- rine20 — the marine radiocarbon age calibration curve (0–55,000 cal BP). *Radiocarbon*, 62, 779–820. doi: 10.1017/RDC.2020.68
- Heinze, C., Gehlen, M., & Land, C. (2006). On the potential of  $^{230}\text{Th}$ ,  $^{231}\text{Pa}$ , and  $^{10}\text{Be}$  for marine rain ratio determinations: A modeling study. *Global Biogeochemical Cycles*, 20(2). doi: 10.1029/2005GB002595
- Henderson, G. M., Heinze, C., Anderson, R. F., & Winguth, A. M. (1999). Global distribution of the  $^{230}\text{Th}$  flux to ocean sediments constrained by GCM modelling. *Deep Sea Research Part I: Oceanographic Research Papers*, 46, 1861–1893. doi: 10.1016/S0967-0637(99)00030-8
- Henry, L. G., McManus, J. F., Curry, W. B., Roberts, N. L., Piotrowski, A. M., & Keigwin, L. D. (2016). North Atlantic ocean circulation and abrupt climate change during the last glaciation. *Science*, 353, 470–474. doi: 10.1126/science.aaf5529
- Hickey, B. (2010). *Reconstructing past flow rates of Southern component water masses using sedimentary  $^{231}\text{Pa}/^{230}\text{Th}$*  (Unpublished doctoral dissertation). University of Oxford.
- Hoffmann, S. S., McManus, J. F., & Swank, E. (2018). Evidence for stable Holocene basin-scale overturning circulation despite variable currents along the deep western boundary of the North Atlantic Ocean. *Geophysical Research Letters*, 45, 13,427–13,436. doi: 10.1029/2018GL080187
- Jeltsch-Thömmes, A., Battaglia, G., Cartapanis, O., Jaccard, S. L., & Joos, F. (2019). Low terrestrial carbon storage at the Last Glacial Maximum: constraints from multi-proxy data. *Climate of the Past*, 15, 849–879. doi: 10.5194/cp-15-849-2019
- Jones, G. A., Johnson, D. A., & Curry, W. B. (1984). High-resolution stratigraphy in late Pleistocene/Holocene sediments of the Vema Channel. *Marine Geology*, 58, 59–87. doi: 10.1016/0025-3227(84)90116-6
- Jonkers, L., Zahn, R., Thomas, A., Henderson, G., Abouchami, W., François, R., Masque, P., Hall, I. R., & Bickert, T. (2015). Deep circulation changes in the central South Atlantic during the past 145 kyr reflected in a combined  $^{231}\text{Pa}/^{230}\text{Th}$ , Neodymium isotope and benthic  $\delta^{13}\text{C}$  record. *Earth and Planetary Science Letters*, 419, 14–21. doi: 10.1016/j.epsl.2015.03.004
- Kalnay, E., Kanamitsu, M., Kistler, R., Collins, W., Deaven, D., Gandin, L., Iredell, M., Saha, S., White, G., Woollen, J., Zhu, Y., Chelliah, M., Ebisuzaki, W., Higgins, W., Janowiak, J., Mo, K. C., Ropelewski, C., Wang, J., Leetmaa, A., Reynolds, R., Jenne, R., & Joseph, D. (1996). The NCEP/NCAR 40-year reanalysis project. *Bulletin of the American Meteorological Society*, 77, 437–472. doi: 10.1175/1520-0477(1996)077<0437:TNYP>2.0.CO;2
- Khatiwala, S. (2023). Fast spin-up of geochemical tracers in ocean circulation and climate models. *Journal of Advances in Modeling Earth Systems*, 15, e2022MS003447. doi: 10.1029/2022MS003447
- Kretschmer, S., Geibert, W., Rutgers van der Loeff, M. M., Schnabel, C., Xu, S., & Mollenhauer, G. (2011). Fractionation of  $^{230}\text{Th}$ ,  $^{231}\text{Pa}$ , and  $^{10}\text{Be}$  induced

- by particle size and composition within an opal-rich sediment of the Atlantic Southern Ocean. *Geochimica et Cosmochimica Acta*, 75, 6971–6987. doi: 10.1016/j.gca.2011.09.012
- Lerner, P., Marchal, O., Lam, P. J., Gardner, W., Richardson, M. J., & Mishonov, A. (2020). A model study of the relative influences of scavenging and circulation on  $^{230}\text{Th}$  and  $^{231}\text{Pa}$  in the western North Atlantic. *Deep Sea Research Part I: Oceanographic Research Papers*, 155, 103–159. doi: 10.1016/j.dsr.2019.103159
- Levier, M., Roy-Barman, M., Foliot, L., Dapoigny, A., & Lacan, F. (2022). Distribution of Pa in the Atlantic sector of the Southern Ocean: Tracking scavenging during water mass mixing along neutral density surfaces. *Deep Sea Research Part I: Oceanographic Research Papers*, 103951. doi: 10.1016/j.dsr.2022.103951
- Li, S., Goldstein, S. L., & Raymo, M. E. (2021). Neogene continental denudation and the beryllium conundrum. *Proceedings of the National Academy of Sciences*, 118, e2026456118. doi: 10.1073/pnas.2026456118
- Lippold, J., Gherardi, J.-M., & Luo, Y. (2011). Testing the  $^{231}\text{Pa}/^{230}\text{Th}$  paleocirculation proxy: A data versus 2D model comparison. *Geophysical Research Letters*, 38(20). doi: 10.1029/2011GL049282
- Lippold, J., Gutjahr, M., Blaser, P., Christner, E., de Carvalho Ferreira, M. L., Mulitza, S., Christl, M., Wombacher, F., Böhm, E., Antz, B., Cartapanis, O., Vogel, H., & Jaccard, S. L. (2016). Deep water provenance and dynamics of the (de)glacial Atlantic meridional overturning circulation. *Earth and Planetary Science Letters*, 445, 68–78. doi: 10.1016/j.epsl.2016.04.013
- Lippold, J., Luo, Y., François, R., Allen, S. E., Gherardi, J., Pichat, S., Hickey, B., & Schulz, H. (2012a). Strength and geometry of the glacial Atlantic Meridional Overturning Circulation. *Nature Geoscience*, 5, 813–816. doi: 10.1038/ngeo1608
- Lippold, J., Mulitza, S., Mollenhauer, G., Weyer, S., Heslop, D., & Christl, M. (2012b). Boundary scavenging at the East Atlantic margin does not negate use of  $^{231}\text{Pa}/^{230}\text{Th}$  to trace Atlantic overturning. *Earth and Planetary Science Letters*, 333–334, 317–331. doi: 10.1016/j.epsl.2012.04.005
- Lippold, J., Pöppelmeier, F., Süfke, F., Gutjahr, M., Goepfert, T. J., Blaser, P., Friedrich, O., Link, J. M., Wacker, L., Rheinberger, S., & Jaccard, S. L. (2019). Constraining the variability of the Atlantic meridional overturning circulation during the Holocene. *Geophysical Research Letters*, 46, 11338–11346. doi: 10.1029/2019GL084988
- Luo, S., & Ku, T.-L. (2004a). On the importance of opal, carbonate, and lithogenic clays in scavenging and fractionating  $^{230}\text{Th}$ ,  $^{231}\text{Pa}$  and  $^{10}\text{Be}$  in the ocean. *Earth and Planetary Science Letters*, 220, 201–211. doi: 10.1016/S0012-821X(04)00027-5
- Luo, S., & Ku, T.-L. (2004b). Reply to Comment on “On the importance of opal, carbonate, and lithogenic clays in scavenging and fractionating  $^{230}\text{Th}$ ,  $^{231}\text{Pa}$



- and  $^{10}\text{Be}$  in the ocean". *Earth and Planetary Science Letters*, 220, 223–229. doi: 10.1016/S0012-821X(04)00029-9
- Luo, Y., François, R., & Allen, S. E. (2010). Sediment  $^{231}\text{Pa}/^{230}\text{Th}$  as a recorder of the rate of the Atlantic meridional overturning circulation: insights from a 2-D model. *Ocean Science*, 6, 381–400. doi: 10.5194/os-6-381-2010
- Luo, Y., Lippold, J., Allen, S. E., Tjiputra, J., Jaccard, S. L., & François, R. (2021). The influence of deep water circulation on the distribution of  $^{231}\text{Pa}$  and  $^{230}\text{Th}$  in the Pacific Ocean. *Earth and Planetary Science Letters*, 554, 116674. doi: 10.1016/j.epsl.2020.116674
- Lynch-Stieglitz, J. (2017). The Atlantic Meridional Overturning Circulation and abrupt climate change. *Annual Review of Marine Science*, 9, 83–104. doi: 10.1146/annurev-marine-010816-060415
- Lynch-Stieglitz, J., Adkins, J. F., Curry, W. B., Dokken, T., Hall, I. R., Herguera, J. C., Hirschi, J. J.-M., Ivanova, E. V., Kissel, C., Marchal, O., Marchitto, T. M., McCave, I. N., McManus, J. F., Mulitza, S., Ninnemann, U., Peeters, F., Yu, E.-F., & Zahn, R. (2007). Atlantic Meridional Overturning Circulation during the Last Glacial Maximum. *Science*, 316(5821), 66–69. doi: 10.1126/science.1137127
- Mahowald, N. M., Albani, S., Kok, J. F., Engelstaeder, S., Scanza, R., Ward, D. S., & Flanner, M. G. (2014). The size distribution of desert dust aerosols and its impact on the Earth system. *Aeolian Research*, 15, 53–71. doi: 10.1016/j.aeolia.2013.09.002
- Mahowald, N. M., Muhs, D. R., Levis, S., Rasch, P. J., Yoshioka, M., Zender, C. S., & Luo, C. (2006). Change in atmospheric mineral aerosols in response to climate: Last glacial period, preindustrial, modern, and doubled carbon dioxide climates. *Journal of Geophysical Research Atmospheres*, 111(10). doi: 10.1029/2005JD006653
- Marchal, O., François, R., & Scholten, J. (2007). Contribution of  $^{230}\text{Th}$  measurements to the estimation of the abyssal circulation. *Deep Sea Research Part I: Oceanographic Research Papers*, 54, 557–585. doi: 10.1016/j.dsr.2007.01.002
- Marchal, O., François, R., Stocker, T. F., & Joos, F. (2000). Ocean thermohaline circulation and sedimentary  $^{231}\text{Pa}/^{230}\text{Th}$  ratio. *Paleoceanography*, 15, 625–641. doi: 10.1029/2000PA000496
- Martin, J. H., Knauer, G. A., Karl, D. M., & Broenkow, W. W. (1987). VERTEX: carbon cycling in the northeast Pacific. *Deep Sea Research Part A: Oceanographic Research Papers*, 34, 267–285. doi: 10.1016/0198-0149(87)90086-0
- Max, L., Nürnberg, D., Chiessi, C. M., Lenz, M. M., & Mulitza, S. (2022). Sub-surface ocean warming preceded Heinrich Events. *Nature Communications*, 13, 4217. doi: 10.1038/s41467-022-31754-x
- McManus, J. F., François, R., Gherardi, J.-M., Keigwin, L. D., & Brown-Leger, S. (2004). Collapse and rapid resumption of Atlantic meridional circulation linked to deglacial climate changes. *Nature*, 428, 834–837. doi: 10.1038/nature02494
- Missiaen, L., Bouttes, N., Roche, D. M., Dutay, J.-C., Quiquet, A., Waelbroeck, C.,

- Pichat, S., & Peterschmitt, J.-Y. (2020a). Carbon isotopes and Pa/Th response to forced circulation changes: a model perspective. *Climate of the Past*, *16*, 867–883. doi: 10.5194/cp-16-867-2020
- Missiaen, L., Menviel, L. C., Meissner, K. J., Roche, D. M., Dutay, J.-C., Bouttes, N., Lhardy, F., Quiquet, A., Pichat, S., & Waelbroeck, C. (2020b). Modelling the impact of biogenic particle flux intensity and composition on sedimentary Pa/Th. *Quaternary Science Reviews*, *240*, 106394. doi: 10.1016/j.quascirev.2020.106394
- Missiaen, L., Waelbroeck, C., Pichat, S., Jaccard, S. L., Eynaud, F., Greenop, R., & Burke, A. (2019). Improving North Atlantic marine core chronologies using  $^{230}\text{Th}$  normalization. *Paleoceanography and Paleoclimatology*, *34*, 1057–1073. doi: 10.1029/2018PA003444
- Mulitza, S., Chiessi, C. M., Schefuß, E., Lippold, J., Wichmann, D., Antz, B., Mackensen, A., Paul, A., Prange, M., Rehfeld, K., Werner, M., Bickert, T., Frank, N., Kuhnert, H., Lynch-Stieglitz, J., Portillo-Ramos, R. C., Sawakuchi, A. O., Schulz, M., Schwenk, T., Tiedemann, R., Vahlenkamp, M., & Zhang, Y. (2017). Synchronous and proportional deglacial changes in Atlantic meridional overturning and northeast Brazilian precipitation. *Paleoceanography*, *32*, 622–633. doi: 10.1002/2017PA003084
- Müller, S. A., Joos, F., Edwards, N. R., & Stocker, T. F. (2006). Water mass distribution and ventilation time scales in a cost-efficient, three-dimensional ocean model. *Journal of Climate*, *19*, 5479–5499. doi: 10.1175/JCLI3911.1
- Negre, C., Zahn, R., Thomas, A. L., Masqué, P., Henderson, G. M., Martínez-Méndez, G., Hall, I. R., & Mas, J. L. (2010). Reversed flow of Atlantic deep water during the Last Glacial Maximum. *Nature*, *468*, 84–88. doi: 10.1038/nature09508
- Ng, H. C., Robinson, L. F., McManus, J. F., Mohamed, K. J., Jacobel, A. W., Ivanovic, R. F., Gregoire, L. J., & Chen, T. (2018). Coherent deglacial changes in western Atlantic Ocean circulation. *Nature Communications*, *9*(1). doi: 10.1038/s41467-018-05312-3
- Ng, H. C., Robinson, L. F., Rowland, G. H., Chen, S. S., & McManus, J. F. (2020). Coupled analysis of seawater and sedimentary  $^{231}\text{Pa}/^{230}\text{Th}$  in the tropical Atlantic. *Marine Chemistry*, *227*, 103894. doi: 10.1016/j.marchem.2020.103894
- Ni, Q., Zhai, X., LaCasce, J. H., Chen, D., & Marshall, D. P. (2023). Full-depth eddy kinetic energy in the global ocean estimated from altimeter and argo observations. *Geophysical Research Letters*, *50*(15), e2023GL103114. doi: 10.1029/2023GL103114
- Nickelsen, L., Keller, D. P., & Oschlies, A. (2015). A dynamic marine iron cycle module coupled to the University of Victoria earth system model: the Kiel marine biogeochemical model 2 for UVic 2.9. *Geoscientific Model Development*, *8*, 1357–1381. doi: 10.5194/gmd-8-1357-2015
- Nielsen, S. B., Jochum, M., Pedro, J. B., Eden, C., & Nuterman, R. (2019). Two-timescale carbon cycle response to an AMOC collapse. *Paleoceanography and*



- Paleoclimatology*, 34, 511–523. doi: 10.1029/2018PA003481
- Okubo, A., Obata, H., Gamo, T., & Yamada, M. (2012).  $^{230}\text{Th}$  and  $^{232}\text{Th}$  distributions in mid-latitudes of the North Pacific Ocean: Effect of bottom scavenging. *Earth and Planetary Science Letters*, 339–340, 139–150. doi: 10.1016/j.epsl.2012.05.012
- Parekh, P., Joos, F., & Müller, S. A. (2008). A modeling assessment of the interplay between aeolian iron fluxes and iron-binding ligands in controlling carbon dioxide fluctuations during Antarctic warm events. *Paleoceanography*, 23(4). doi: 10.1029/2007PA001531
- Pavia, F. J., Anderson, R. F., Black, E. E., Kipp, L. E., Vivancos, S. M., Fleisher, M. Q., Charette, M. A., Sanial, V., Moore, W. S., Hult, M., Lu, Y., Cheng, H., Zhang, P., & Edwards, R. L. (2019). Timescales of hydrothermal scavenging in the South Pacific Ocean from  $^{234}\text{Th}$ ,  $^{230}\text{Th}$ , and  $^{228}\text{Th}$ . *Earth and Planetary Science Letters*, 506, 146–156. doi: 10.1016/j.epsl.2018.10.038
- Pavia, F. J., Anderson, R. F., Pinedo-Gonzalez, P., Fleisher, M. Q., Brzezinski, M. A., & Robinson, R. S. (2020). Isopycnal transport and scavenging of  $^{230}\text{Th}$  and  $^{231}\text{Pa}$  in the Pacific Southern Ocean. *Global Biogeochemical Cycles*, 34, e2020GB006760. doi: 10.1029/2020GB006760
- Pöppelmeier, F., Gutjahr, M., Blaser, P., Schulz, H., Süfke, F., & Lippold, J. (2021). Stable Atlantic deep water mass sourcing on glacial-interglacial timescales. *Geophysical Research Letters*, 48, e2021GL092722. doi: 10.1029/2021GL092722
- Regelous, M., Turner, S. P., Elliott, T. R., Rostami, K., & Hawkesworth, C. J. (2004). Measurement of femtogram quantities of protactinium in silicate rock samples by multicollector inductively coupled plasma mass spectrometry. *Analytical Chemistry*, 76, 3584–3589. doi: 10.1021/ac030374l
- Rempfer, J., Stocker, T. F., Joos, F., Dutay, J.-C., & Siddall, M. (2011). Modelling Nd-isotopes with a coarse resolution ocean circulation model: Sensitivities to model parameters and source/sink distributions. *Geochimica et Cosmochimica Acta*, 75, 5927–5950. doi: 10.1016/j.gca.2011.07.044
- Rempfer, J., Stocker, T. F., Joos, F., Lippold, J., & Jaccard, S. L. (2017). New insights into cycling of  $^{231}\text{Pa}$  and  $^{230}\text{Th}$  in the Atlantic Ocean. *Earth and Planetary Science Letters*, 468, 27–37. doi: 10.1016/j.epsl.2017.03.027
- Repschläger, J., Zhao, N., Rand, D., Lisiecki, L., Muglia, J., Mulitza, S., Schmittner, A., Cartapanis, O., Bauch, H. A., Schiebel, R., & Haug, G. H. (2021). Active North Atlantic deepwater formation during Heinrich Stadial 1. *Quaternary Science Reviews*, 270, 107145. doi: 10.1016/j.quascirev.2021.107145
- Ritz, S. P., Stocker, T. F., & Joos, F. (2011). A coupled dynamical ocean-energy balance atmosphere model for paleoclimate studies. *Journal of Climate*, 24, 349–375. doi: 10.1175/2010JCLI3351.1
- Roberts, N. L., McManus, J. F., Piotrowski, A. M., & McCave, I. N. (2014). Advection and scavenging controls of Pa/Th in the northern NE Atlantic. *Paleoceanography*, 29, 668–679. doi: 10.1002/2014PA002633

- Roth, R., Ritz, S. P., & Joos, F. (2014). Burial-nutrient feedbacks amplify the sensitivity of atmospheric carbon dioxide to changes in organic matter remineralisation. *Earth System Dynamics*, 5, 321–343. doi: 10.5194/esd-5-321-2014
- Roy-Barman, M., Foliot, L., Douville, E., Leblond, N., Gazeau, F., Bressac, M., Wagener, T., Ridame, C., Desboeufs, K., & Guieu, C. (2021). Contrasted release of insoluble elements (Fe, Al, rare earth elements, Th, Pa) after dust deposition in seawater: a tank experiment approach. *Biogeosciences*, 18, 2663–2678. doi: 10.5194/bg-18-2663-2021
- Roy-Barman, M., Thil, F., Bordier, L., Dapoigny, A., Foliot, L., Ayrault, S., Lacan, F., Jeandel, C., Pradoux, C., & Garcia-Solsona, E. (2019). Thorium isotopes in the Southeast Atlantic Ocean: Tracking scavenging during water mass mixing along neutral density surfaces. *Deep Sea Research Part I: Oceanographic Research Papers*, 149, 103042. doi: 10.1016/j.dsr.2019.05.002
- Sarmiento, J. L., & Gruber, N. (2006). *Ocean biogeochemical dynamics*. Woodstock: Princeton University Press.
- Sasaki, Y., Kobayashi, H., & Oka, A. (2022). Global simulation of dissolved  $^{231}\text{Pa}$  and  $^{230}\text{Th}$  in the ocean and the sedimentary  $^{231}\text{Pa}/^{230}\text{Th}$  ratios with the ocean general circulation model COCO ver4.0. *Geoscientific Model Development*, 15, 2013–2033. doi: 10.5194/gmd-15-2013-2022
- Scheen, J. (2020). *Effect of changing ocean circulation on deep ocean temperature in the last millennium: code* [Software]. Zenodo. (v1.1.0) doi: 10.5281/zenodo.4022947
- Scheen, J., Mishonov, A. V., Richardson, M. J., & Gardner, W. D. (2024b). *Code for: “Promising regions for detecting the overturning circulation in Atlantic Pa/Th: a model-data comparison”* [Software]. Zenodo. (v1.0.0) doi: 10.5281/zenodo.10622404
- Scheen, J., Pöppelmeier, F., & Stocker, T. F. (2024a). *Simulation output data for: “Promising regions for detecting the overturning circulation in Atlantic Pa/Th: a model-data comparison”* [Dataset]. Zenodo. (v1.0.0) doi: 10.5281/zenodo.10621275
- Schmiedl, G., & Mackensen, A. (1997). Late Quaternary paleoproductivity and deep water circulation in the eastern South Atlantic Ocean: Evidence from benthic foraminifera. *Palaeogeography, Palaeoclimatology, Palaeoecology*, 130(1), 43–80. doi: 10.1016/S0031-0182(96)00137-X
- Schmittner, A. (2005). Decline of the marine ecosystem caused by a reduction in the Atlantic overturning circulation. *Nature*, 434, 628–633. doi: 10.1038/nature03476
- Siddall, M., Henderson, G. M., Edwards, N. R., Frank, M., Müller, S. A., Stocker, T. F., & Joos, F. (2005).  $^{231}\text{Pa}/^{230}\text{Th}$  fractionation by ocean transport, biogenic particle flux and particle type. *Earth and Planetary Science Letters*, 237, 135–155. doi: 10.1016/j.epsl.2005.05.031
- Stocker, T. F., Timmermann, A., Renold, M., & Timm, O. (2007). Effects of salt compensation on the climate model response in simulations of large changes

- of the Atlantic Meridional Overturning Circulation. *Journal of Climate*, *20*, 5912–5928. doi: 10.1175/2007JCLI1662.1
- Süfke, F., Lippold, J., & Happel, S. (2018). Improved separation of Pa from Th and U in marine sediments with TK400 Resin. *Analytical Chemistry*, *90*, 1395–1401. doi: 10.1021/acs.analchem.7b04723
- Süfke, F., Schulz, H., Scheen, J., Szidat, S., Regelous, M., Blaser, P., Pöppelmeier, F., Goepfert, T. J., Stocker, T. F., & Lippold, J. (2020). Inverse response of  $^{231}\text{Pa}/^{230}\text{Th}$  to variations of the Atlantic meridional overturning circulation in the North Atlantic intermediate water. *Geo-Marine Letters*, *40*, 75–87. doi: 10.1007/s00367-019-00634-7
- Süfke, F., Pöppelmeier, F., Goepfert, T. J., Regelous, M., Koutsodendris, A., Blaser, P., Gutjahr, M., & Lippold, J. (2019). Constraints on the North-western Atlantic deep water circulation from  $^{231}\text{Pa}/^{230}\text{Th}$  during the last 30,000 years. *Paleoceanography and Paleoclimatology*, *34*, 1945–1958. doi: 10.1029/2019PA003737
- Tessin, A. C., & Lund, D. C. (2013). Isotopically depleted carbon in the mid-depth South Atlantic during the last deglaciation. *Paleoceanography*, *28*, 296–306. doi: 10.1002/palo.20026
- Tschumi, T., Joos, F., & Parekh, P. (2008). How important are Southern Hemisphere wind changes for low glacial carbon dioxide? a model study. *Paleoceanography*, *23*(4). doi: 10.1029/2008PA001592
- van Hulten, M., Dutay, J.-C., & Roy-Barman, M. (2018). A global scavenging and circulation ocean model of thorium-230 and protactinium-231 with improved particle dynamics (NEMO-ProThorP 0.1). *Geoscientific Model Development*, *11*, 3537–3556. doi: 10.5194/gmd-11-3537-2018
- Vencharutti, C., van der Loeff, M. R., & Stimac, I. (2011). Scavenging of  $^{231}\text{Pa}$  and thorium isotopes based on dissolved and size-fractionated particulate distributions at Drake Passage (ANTXXIV-3). *Deep Sea Research Part II: Topical Studies in Oceanography*, *58*, 2767–2784. doi: 10.1016/j.dsr2.2010.10.040
- Voigt, I., Cruz, A. P. S., Mulitza, S., Chiessi, C. M., Mackensen, A., Lippold, J., Antz, B., Zabel, M., Zhang, Y., Barbosa, C. F., & Tisserand, A. A. (2017). Variability in mid-depth ventilation of the western Atlantic Ocean during the last deglaciation. *Paleoceanography*, *32*, 948–965. doi: 10.1002/2017PA003095
- Waelbroeck, C., Lougheed, B. C., Vazquez Riveiros, N., Missiaen, L., Pedro, J., Dokken, T., Hajdas, I., Wacker, L., Abbott, P., Dumoulin, J.-P., Thil, F., Eynaud, F., Rossignol, L., Fersi, W., Albuquerque, A. L., Arz, H., Austin, W. E. N., Came, R., Carlson, A. E., Collins, J. A., Dennielou, B., Desprat, S., Dickson, A., Elliot, M., Farmer, C., Giraudeau, J., Gottschalk, J., Hendriks, J., Hughen, K., Jung, S., Knutz, P., Lebreiro, S., Lund, D. C., Lynch-Stieglitz, J., Malaizé, B., Marchitto, T., Martínez-Méndez, G., Mollenhauer, G., Naughton, F., Nave, S., Nürnberg, D., Oppo, D., Peck, V., Peeters, F. J. C., Penaud, A., Portillo-Ramos, R. d. C., Repschläger, J., Roberts, J., Rühlemann, C., Salgueiro, E., Sanchez Goni, M. F., Schönfeld, J., Scussolini,

- P., Skinner, L. C., Skonieczny, C., Thornalley, D., Toucanne, S., Rooij, D. V., Vidal, L., Voelker, A. H. L., Wary, M., Weldeab, S., & Ziegler, M. (2019). Consistently dated Atlantic sediment cores over the last 40 thousand years. *Scientific Data*, 6, 165. doi: 10.1038/s41597-019-0173-8
- Waelbroeck, C., Pichat, S., Böhm, E., Lougheed, B. C., Faranda, D., Vrac, M., Misiaen, L., Vazquez Riveiros, N., Burckel, P., Lippold, J., Arz, H. W., Dokken, T., Thil, F., & Dapoigny, A. (2018). Relative timing of precipitation and ocean circulation changes in the western equatorial Atlantic over the last 45 kyr. *Climate of the Past*, 14, 1315–1330. doi: 10.5194/cp-14-1315-2018
- Wollenburg, J. E., Knies, J., & Mackensen, A. (2004). High-resolution paleoproductivity fluctuations during the past 24 kyr as indicated by benthic foraminifera in the marginal Arctic Ocean. *Palaeogeography, Palaeoclimatology, Palaeoecology*, 204(3), 209–238. doi: 10.1016/S0031-0182(03)00726-0
- Zhang, X., Yang, W., Qiu, Y., & Zheng, M. (2021). Adsorption of Th and Pa onto particles and the effect of organic compounds in natural seawater. *Journal of Oceanology and Limnology*, 39, 2209–2219. doi: 10.1007/s00343-021-0297-5
- Zhuang, J., Dussin, R., Huard, D., Bourgault, P., Banihirwe, A., Raynaud, S., Malevich, B., Schupfner, M., Filipe, Levang, S., Gauthier, C., Jüling, A., Almansi, M., RichardScottOZ, RondeauG, Rasp, S., Smith, T. J., Stachelek, J., Plough, M., Pierre, Bell, R., Caneill, R., & Li, X. (2023). *xESMF: Universal regridding for geospatial data* [Software]. Zenodo. doi: 10.5281/zenodo.8356796